A Multidimensional Spectral Description of Ocean Variability

CIMARRON WORTHAM

Applied Physics Laboratory, University of Washington, Seattle, Washington

CARL WUNSCH

Department of Earth and Planetary Sciences, Harvard University, Cambridge, Massachusetts

(Manuscript received 14 May 2013, in final form 30 September 2013)

ABSTRACT

An updated empirical, analytical model for the frequency and wavenumber distribution of balanced motion in the ocean is presented. The spectrum model spans periods longer than the inertial but shorter than a decade and wavelengths between 100 and 10 000 km. Assuming geostrophic dynamics, a spectrum model for the streamfunction is constructed to be consistent with a range of observations, including sea surface height from satellite altimetry, velocity from moored and shipboard instruments, and temperature from moorings. First-order characteristics of the observed spectra, including amplitude and spectral moments, vary slowly geographically. The spectrum model is horizontally anisotropic, accommodating observations that zonal wavenumber–frequency spectra are dominated by a "nondispersive line." Qualitative and quantitative agreement is found with one-dimensional frequency and wavenumber spectra and observed vertical profiles of variance. Illustrative application is made of the model spectrum to observing-system design, data mapping, and uncertainty estimation for trends.

1. Introduction

Data describing the general circulation of the ocean are extremely noisy (e.g., Ganachaud 2003; Zhai et al. 2011). The extraction of signals from such observations requires a detailed knowledge of the space and time scales of the stochastic variability. Of course, one person's noise is another's signal. Stochastic variability is itself a part of the ocean circulation and is of great interest in its own right. Since the time of the Mid-Ocean Dynamics Experiment (MODE Group 1978), the oceanographic community has collected countless measurements showing variability of different types (including velocity, temperature, and surface elevation) in time and/or space. Synthesizing those observations of ocean variability into a quantitatively useful form is a considerable challenge. The specific availability of high-accuracy near-global altimetry since 1992 has sparked a number of partial synthesis efforts, including estimates of the frequency (e.g., Le Traon 1990; Lin et al. 2008; Hughes and Williams 2010) and wavenumber (e.g., Stammer 1997; Le Traon et al. 2008; Xu and Fu 2012) spectrum. A first attempt at the desired combined frequency–wavenumber spectrum was made by Zang and Wunsch (2001) and Wunsch (2010).

The purpose of this paper is to extend these earlier efforts so as to construct a full four-dimensional (three wavenumbers plus frequency) spectral representation of oceanic variability, along with an estimate of the extent to which it is likely both accurate and useful. A wide range of observations are used, including sea surface height (SSH) from altimetry, temperature and velocity time series from moored instruments, and velocity from shipboard current meters. As a consequence of the available observational record, the resulting description extends from periods longer than the inertial to about a decade and wavelengths from about 100 km to several thousands of kilometers. As a shorthand, variability in these ranges will be referred to as "balanced motions," suggesting the expectation of near geostrophy in their physics.

Altimetric data provide the only continuous, near-global record of ocean variability with a simple dynamical interpretation (owing to the complex boundary layers at the air–sea interface, sea surface temperature, salinity, and color are much more difficult to interpret).

Corresponding author address: Cimarron Wortham, Applied Physics Laboratory, University of Washington, 1013 NE 40th St., Seattle, WA 98105.
E-mail: cwortham@uw.edu

DOI: 10.1175/JPO-D-13-0113.1

As such, the altimetric record provides the backbone of the resulting spectral model, jointly covering horizontal wavenumber and frequency.

Like all data, the altimetric record contains complicated structures from measurement noise and from the elaborate data processing involved in estimating SSH from the raw observations. Accounting for these complexities has to be part of the synthesis effort. The greatest problem with reliance on SSH is in understanding how it reflects motions interior to the ocean. Although in the geostrophic limit employed here, boundary layer phenomena are not of first-order concern, the partition of SSH into barotropic and baroclinic structures, expected to be a function of wavenumber/frequency and geography, is perhaps the greatest theoretical and observational challenge.

To address the problem, the vertical structure of variability is inferred where possible from moored instruments. Unfortunately, the number of moored instruments with sufficient duration and vertical resolving power is very limited (Scott et al. 2010). What data are available are used in combination with basic theoretical ideas to construct a strawman spectrum. Some of the theoretical considerations are put in context by employing an oceanic general circulation model [GCM; called Estimating the Circulation and Climate of the Ocean, phase 2 (ECCO2)], with the strong caveat that the same very small database renders nearly impossible tests of model skill.

To a degree, this paper attempts to do for oceanic balanced motions what the Garrett–Munk (Garrett and Munk 1972, 1975) spectrum did for the internal-wave band. Their work has served as a tool for interpreting experimental results, highlighted gaps in the observational record, and inspired theoretical efforts to explain their description. At the end of this paper, the utility of the present spectrum model[1] will be demonstrated through application to the important problem of oceanic trend determination. The spectrum model can be used to predict vertical and horizontal coherence between measurements. Many elements of the result are also in need of theoretical explanation, and perhaps progress in that direction will be a result.

2. Dynamic model for balanced motion

Zang (2000) took the linearized, quasigeostrophic, β-plane equations as a basic dynamical model and showed that the spectra of horizontal velocity (u, v), vertical velocity w, vertical displacement ζ, density ρ, potential temperature θ, and pressure p can all be derived from the spectrum of the geostrophic streamfunction $\psi = p/\rho_0 f_0$, where ρ_0 is the reference density and f_0 is the local Coriolis parameter. In this section, the basic dynamical model introduced by Zang (2000) is reviewed and the implied relations between observable spectra are recorded. Separating the variables,

$$\psi(x,y,z,t) = \sum_{n=0}^{\infty} \psi_n(x,y,z,t) \tag{1}$$

$$= \sum_{n=0}^{\infty} \Psi_n(x,y,t) F_n(z), \tag{2}$$

where the orthonormal vertical modes $F_n(z)$ satisfy (e.g., Gill 1982)

$$\frac{d}{dz}\left[\frac{f_0^2}{N^2(z)}\frac{dF}{dz}\right] + \gamma^2 F(z) = 0, \tag{3}$$

where $N(z)$ is the buoyancy frequency. With its boundary conditions, (3) forms a Sturm–Liouville eigenvalue problem whose eigenfunctions $F_n(z)$, $0 \le n < \infty$, represent the vertical structure of horizontal velocity free modes in the ocean and whose eigenvalues are related to the deformation radius $L_d = 1/\gamma$.

The vertical velocity is proportional to another vertical mode $G_n(z)$:

$$G_n(z) = \frac{1}{N^2(z)}\frac{dF_n(z)}{dz}, \tag{4}$$

satisfying

$$\frac{d^2 G_n(z)}{dz^2} + \gamma_n^2 \frac{N^2(z)}{f_0^2} G_n(z) = 0, \tag{5}$$

with appropriate boundary conditions.

Equations (3) and (4) are typically derived under the basic textbook theory (BTT) assumptions of linearity, resting mean state, and flat-bottom and rigid-lid boundary conditions. Although these conditions are not satisfied in the real ocean, solutions to (3) form a complete set, capable of describing any vertical structure. However, if the assumptions are violated, the representation may be very inefficient. Alternative surface boundary conditions account for Ekman pumping (Philander 1978) or nonlinear buoyancy advection, as in surface quasigeostrophic (SQG) theory (Lapeyre and Klein 2006). Alternative bottom boundary conditions account for bathymetry (Tailleux and McWilliams 2001;

[1] The terminology spectrum model is used to distinguish the results from a spectral model (GCM formulated in spectral space) or model spectrum (spectrum of GCM output).

Killworth and Blundell 2004). Important modifications to (3) will be discussed in section 5.

Treating the streamfunction as a sum of plane waves, the full streamfunction in mode n is

$$\psi_n(x,y,z,t) = \int_0^\infty \int_{-\infty}^\infty \int_{-\infty}^\infty \tilde{\psi}(k,l,\omega,n) F_n(z) e^{i2\pi(kx+ly-\omega t)}\, dk\, dl\, d\omega, \tag{6}$$

where $\tilde{\psi}(k,l,\omega,n)$ is the Fourier transform of the streamfunction. Note that cyclic frequencies and wavenumbers are being used. For a generic variable $\chi_n(x, y, z, t)$, the nth mode is

$$\chi_n(x,y,z,t) = \int_0^\infty \int_{-\infty}^\infty \int_{-\infty}^\infty \tilde{\chi}(k,l,\omega,z,n)\tilde{\psi}(k,l,\omega,n) e^{i2\pi(kx+ly-\omega t)}\, dk\, dl\, d\omega. \tag{7}$$

Zang and Wunsch (2001) derived the characteristic functions $\tilde{\chi}(k,l,\omega,z,n)$, and the representations are

$$\tilde{p}(k,l,\omega,z,n) = \rho_0 f_0 F_n(z), \tag{8}$$

$$\tilde{u}(k,l,\omega,z,n) = -i2\pi l F_n(z), \tag{9}$$

$$\tilde{v}(k,l,\omega,z,n) = i2\pi k F_n(z), \tag{10}$$

$$\tilde{w}(k,l,\omega,z,n) = i2\pi\omega f_0 G_n(z), \tag{11}$$

$$\tilde{\rho}(k,l,\omega,z,n) = -\frac{\rho_0 f_0}{g} N^2(z) G_n(z), \tag{12}$$

$$\tilde{\zeta}(k,l,\omega,z,n) = -f_0 G_n(z), \quad \text{and} \tag{13}$$

$$\tilde{\theta}(k,l,\omega,z,n) = f_0 \frac{\partial\theta_0}{\partial z} G_n(z), \tag{14}$$

where θ_0 is the time-mean potential temperature.

Different frequencies, wavenumbers, and vertical modes are assumed to be uncorrelated, assuring horizontal spatial and temporal stationarity. Among other phenomena, these assumptions ignore the possible presence of coherent mesoscale features (Chelton et al. 2011). Because they are represented by phase-locked modes, an "changed" variance is expected relative to that of a stationary random wave field. While Chelton et al. (2011) show the presence of coherent features in the SSH record, other forms of variability are also plainly present in the records. A more complete description than the one to be obtained here eventually needs to account for both coherent and incoherent (statistically stationary, random) components of the variability.

A spectrum model

The three-dimensional frequency and wavenumber spectrum for the mode-n streamfunction is

$$\Phi_\psi(k,l,\omega,n) = \langle |\tilde{\psi}(k,l,\omega,n|^2 \rangle, \tag{15}$$

where angle brackets represent an ensemble average. For other variables, the spectrum at depth z and mode n can be calculated from the spectrum of the streamfunction and the appropriate characteristic function:

$$\Phi_\chi(k,l,\omega,z,n) = |\tilde{\chi}(k,l,\omega,z,n)|^2 \Phi_\psi(k,l,\omega,n), \tag{16}$$

and can be summed over all vertical modes:

$$\Phi_\chi(k,l,\omega,z) = \sum_{n=0}^{\infty} |\tilde{\chi}(k,l,\omega,z,n)|^2 \Phi_\psi(k,l,\omega,n). \tag{17}$$

Two- or one-dimensional spectra can be obtained by integrating the three-dimensional spectrum over one or two dimensions. Notation for the one-, two-, or three-dimensional spectra of a variable χ can be quite cumbersome. The term $\Phi_\chi(k, l, \omega, z)$ is written for the spectrum of χ at depth z, and the arguments (k, l, ω) denote the dimensionality. For example, the two-dimensional wavenumber spectrum is

$$\Phi_\chi(k,l,z) = \int_0^\infty \Phi_\chi(k,l,\omega,z)\, d\omega. \tag{18}$$

Similarly,

$$\Phi_\chi(l,z) = \int_0^\infty \int_{-\infty}^\infty \Phi_\chi(k,l,\omega,z)\, dk\, d\omega. \tag{19}$$

For simplicity, and in the absence of observational evidence to the contrary (Zang and Wunsch 2001), we assume that the shape of the spectrum in horizontal wavenumber–frequency space is independent of mode number. Accordingly, a streamfunction spectrum of the form

$$\Phi_\psi(k,l,\omega,n;\phi,\lambda) = \Phi_\psi(k,l,\omega;\phi,\lambda)E(n)I(\phi,\lambda) \quad (20)$$

is proposed, where $\Phi_\psi(k, l, \omega; \phi, \lambda)$ is the three-dimensional wavenumber–frequency spectrum, and changes slowly with latitude ϕ and longitude λ. The term $E(n)$ represents the relative contribution from each vertical mode n. The term $I(\phi, \lambda)$ is a normalization factor:

$$I(\phi,\lambda) = \mathrm{EKE}\left[\int_0^\infty\int_{-\infty}^\infty\int_{-\infty}^\infty \frac{1}{2}(|\tilde{u}|^2 + |\tilde{v}|^2)\Phi_\psi(k,l,\omega;\phi,\lambda)\,dk\,dl\,d\omega \sum_{n=0}^\infty E(n)\right]^{-1}, \quad (21)$$

where EKE is the surface eddy kinetic energy estimated from altimetry (Stammer 1997). With this normalization, (20) matches the observed surface eddy kinetic energy.

Many applications of the spectrum model rely on the Wiener–Khinchin theorem, showing that the Fourier transform of the stationary process power spectrum is the covariance function:

$$\mathrm{Cov}(r_x, r_y, \tau) = \int_0^\infty\int_{-\infty}^\infty\int_{-\infty}^\infty \Phi_\chi(k,l,\omega)e^{i2\pi(kr_x+lr_y+\omega\tau)}\,dk\,dl\,d\omega, \quad (22)$$

where r_x, r_y, and τ are the displacements in the zonal, meridional, and temporal directions, respectively. Normalizing by the signal variance gives the correlation function

$$\mathrm{Cor}(r_x, r_y, \tau) = \frac{\mathrm{Cov}(r_x, r_y, \tau)}{\sigma_\chi^2}, \quad (23)$$

where σ_χ^2 is the variance of χ. For standard one-dimensional autocovariances

$$\mathrm{Cov}(r_x) = \int_0^\infty\int_{-\infty}^\infty\int_{-\infty}^\infty \Phi_\chi(k,l,\omega)e^{i2\pi kr_x}\,dk\,dl\,d\omega. \quad (24)$$

For two time series (possibly representing different quantities) at locations (x, y, z) and $(x + r_x, y + r_y, z')$, the cross spectrum between $\chi(x, y, z, t)$ and $\Upsilon(x + r_x, y + r_y, z', t)$ is

$$\Phi_{\chi\Upsilon}(\omega;r_x,r_y,z,z') = \sum_{n=0}^\infty\int_{-\infty}^\infty\int_{-\infty}^\infty \tilde{\chi}(k,l,\omega,z,n)\tilde{\Upsilon}^*(k,l,\omega,z',n)\Phi_\psi(k,l,\omega,n)e^{i2\pi(kr_x+lr_y)}\,dk\,dl, \quad (25)$$

where $\tilde{\chi}$ and $\tilde{\Upsilon}$ are the characteristic functions for the two variables and an asterisk indicates the complex conjugate. The coherence is

$$\mathrm{Coh}(\omega;r_x,r_y,z,z') = \frac{\Phi_{\chi\Upsilon}(\omega;r_x,r_y,z,z')}{\sqrt{\Phi_\chi(\omega,z)\Phi_\Upsilon(\omega,z)}}. \quad (26)$$

Spatial variation in the spectral shape is neglected in the coherence calculation. Observations out to periods of a few years show little correlation between measurements separated by more than a few hundred kilometers (Stammer 1997). While significant coherence over long distances may exist at very low frequencies (because of, e.g, a shift in gyre location over decades), we are not aware of any supporting observations.

3. Observed spectrum

From the earlier work cited above, it is clear from the outset that, unlike the internal-wave case, a truly universal spectral description of balanced motions is impossible. Many qualitative aspects of the spectrum vary geographically including eddy kinetic energy levels, which change by over four orders of magnitude (Stammer 1997). The slowly varying geographical factors attempt to accommodate this spatial nonstationarity in as simple a fashion as possible.

Oceanic spectra, grouped by data type, are now examined.

a. Altimetry

1) MULTIDIMENSIONAL SPECTRAL SHAPE

The most complete observations of the spectrum of ocean variability come from the Archiving, Validation, and Interpretation of Satellite Oceanographic data (AVISO) multimission mapped altimetry product (Ducet et al. 2000). We use the ''reference'' version, in which data from two simultaneous satellite altimeter missions were merged and mapped onto a 1/3° Mercator grid at 7-day intervals for the period October 1992–December 2010; the 1993–99 mean was removed at each grid point. From the AVISO product, the three-dimensional power spectrum can be estimated as discussed in Wortham (2013).

One striking characteristic of the resulting spectrum is its dominance almost everywhere by a ''nondispersive'' straight line in zonal wavenumber–frequency space (Wunsch 2009, 2010; Ferrari and Wunsch 2010; Early et al. 2011) with phase speed independent of wavelength or frequency over a wide range. This phase speed is faster than the standard long Rossby wave prediction at most latitudes (Chelton and Schlax 1996) and has attracted wide theoretical attention. The nondispersive line dominates at wavelengths larger than about 500 km and periods longer than 2 weeks at 10° or longer than 2 months at 40°. At shorter wavelengths, the anisotropy diminishes, and the spectrum appears to approach an isotropic power law in wavenumber, although the resolution of the gridded altimetry product is insufficient to make a definitive statement at wavelengths shorter than 200 km. At high frequency, the spectrum approaches approximate power laws in both frequency and wavenumber.

2) Dominant periods and wavelengths

Display and interpretation of multidimensional spectral structures is extremely challenging, and some simplified representations are useful. For example, Jacobs et al. (2001) estimated zonal wavelength, meridional wavelength, and period by fitting an exponential to the binned covariance function estimated from altimetry. Here, spectral moments (Vanmarcke 2010) are used. Define

$$\langle \omega^q \rangle = \int_0^\infty \omega^q \Phi_\eta(\omega)\, d\omega \Big/ \int_0^\infty \Phi_\eta(\omega)\, d\omega, \tag{27}$$

$$\langle k^q \rangle = \int_0^\infty k^q [\Phi_\eta(k) + \Phi_\eta(-k)]\, dk \Big/ \int_0^\infty [\Phi_\eta(k) + \Phi_\eta(-k)]\, dk, \quad \text{and} \tag{28}$$

$$\langle l^q \rangle = \int_0^\infty l^q [\Phi_\eta(l) + \Phi_\eta(-l)]\, dl \Big/ \int_0^\infty [\Phi_\eta(l) + \Phi_\eta(-l)]\, dl, \tag{29}$$

for integer q. For k and l, the moments of the spectrum are averaged over both positive and negative wavenumbers[2] and are estimated globally on a 5° grid as follows: for each grid point, using SSH maps within a box 10° in longitude by 30° latitude, the spatial mean and linear trend in latitude and longitude are removed at each time step, and the three-dimensional FFT is computed for the region. The k–l–ω spectra are computed from the FFT, averaged over three neighboring frequency–wavenumber bands. Other windowing functions did not significantly alter the results. See Wortham (2013) for further details.

Maps of the inverse of the first moments of frequency and wavenumber are shown (Fig. 1). For the zonal wavenumber, hatching indicates a dominance of eastward propagation. For the meridional wavenumber, hatching indicates a dominance of poleward propagation. Dominant periods increase from less than 100 days near the equator to about 300 days at 40°. Dominant zonal wavelengths decrease from about 1400 km near the equator to 750 km at 40°, while meridional wavelengths range from 900 to 650 km. Such maps provide a quantitative point of comparison for the spectrum model in section 4.

The AVISO mapping procedure imposes space and time correlation scales on the data product (Ducet et al. 2000), which impact estimated dominant periods and wavelengths. Specifically, AVISO frequency spectra have a steeper high-frequency roll-off than other observations, resulting in longer dominant periods (Chiswell and Rickard 2008). Despite such limitations, the AVISO gridded altimetry is used since it allows for straightforward computation of zonal and meridional spectra.

3) Spectral slopes

While the gridded altimetry provides a useful tool for studying the three-dimensional SSH spectrum and its global variations, the AVISO mapping procedure significantly alters the shape of the resulting spectrum (Wortham 2013). Therefore, we now consider the spectrum from the Ocean Topography Experiment (TOPEX)/Poseidon alongtrack altimetry, rather than the gridded altimetry product, using the multitaper estimate as with all one-dimensional records in this paper.

Observed wavenumber spectra are shown for two locations in the North Pacific Ocean (Fig. 2): a high-energy region of the Kuroshio Extension centered at 35°N, 168°E and a relatively low-energy region of the subtropical gyre centered at 35°N, 222°E. In the high-energy region, the spectral slope in the 100–200-km wavelength band is close to k^{-4}, while the spectral slope is significantly flatter in the low-energy region, closer to k^{-2}. In the high-wavenumber tails, the spectrum flattens to k^{-1}

[2] Alternatively, we might calculate the moments for positive and negative wavenumber independently, as in Wunsch (2010).

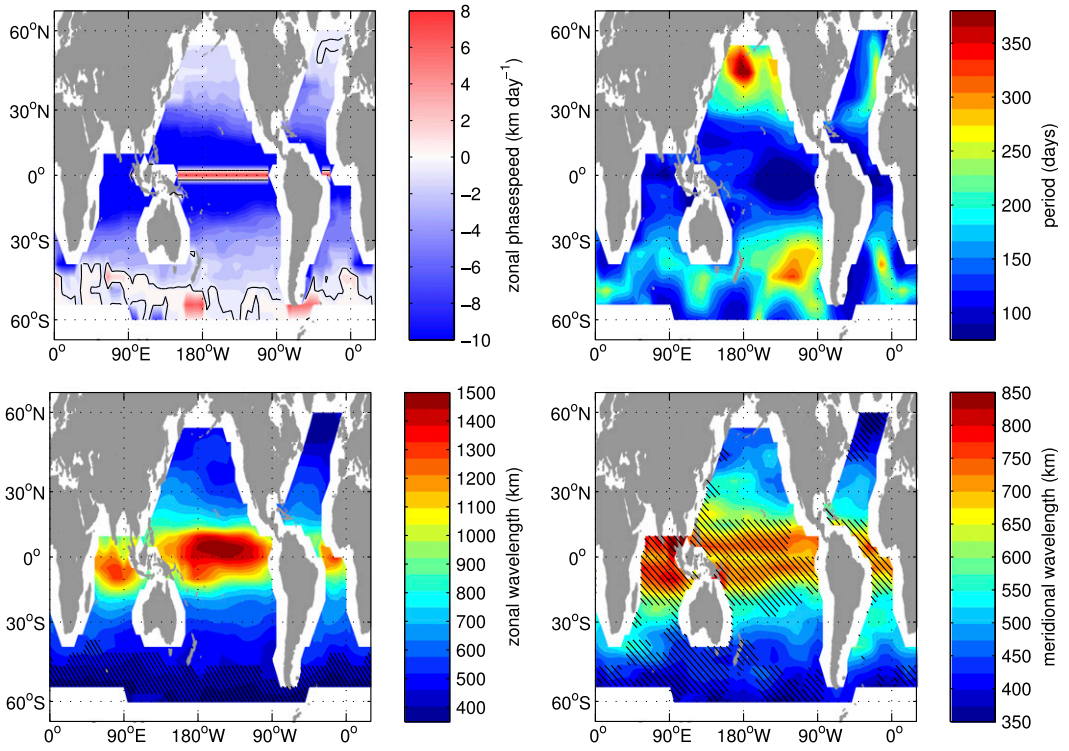

FIG. 1. (top left) Dominant phase speed, (top right) period, (bottom left) zonal wavelength, and (bottom right) meridional wavelength based on the inverse of the first moment of the one-dimensional spectra. For zonal wavelength, the hatched area indicates regions where eastward propagation dominates; elsewhere, westward propagation dominates. For meridional wavelength, the hatched area indicates regions where poleward propagation dominates; elsewhere, equatorward propagation dominates.

at both locations. For reference, we also show the wavenumber spectrum from the AVISO gridded altimetry, linearly interpolated along the satellite track. The spectrum from the AVISO gridded altimetry is steeper than that from the ungridded altimetry at wavelengths shorter than about 250 km.

Wunsch and Stammer (1995), Le Traon et al. (2008), and Xu and Fu (2012) have fit power laws to the high-wavenumber SSH spectrum. High-wavenumber spectral slopes vary geographically, but the true values remain uncertain. Much of the high-wavenumber tail is due to noise, but the extent to which the altimetric wavenumber

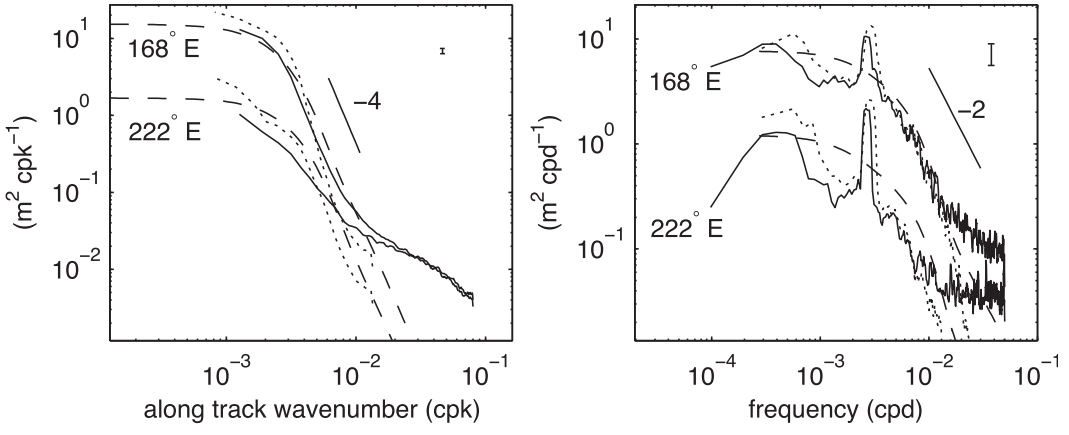

FIG. 2. (left) Alongtrack wavenumber and (right) frequency spectra from tracks spanning from 30° to 40°N at the indicated longitude (solid line). Dashed lines show the spectrum model at each location, discussed in section 4. Dotted lines show the spectra from AVISO gridded altimetry, interpolated along the satellite track. Vertical bars indicate the 95% confidence interval.

spectrum is contaminated by noise is a matter of debate. Stammer (1997) concluded, based on filtered alongtrack wavenumber spectra from altimetry, that SSH spectra displayed a remarkably universal k^{-4} power law at wavelengths shorter than 400 km. Xu and Fu (2012) estimated spectral slopes varying from $k^{-4.5}$ in high-energy regions to k^{-2} in low-energy subtropics and k^{-1} in the tropics.

For SSH frequency spectral slopes, Stammer (1997) found that different regions (tropical, high, and low energy) behaved differently in the low-frequency limit, but all approached an ω^{-2} power law by around 30-day periods. The frequency spectrum of sea surface slope (proportional to velocity) was found to have an almost white long-period plateau, $\omega^{-1/2}$ power-law relation for periods between 40 and 250 days, and roughly an ω^{-2} relation for shorter periods. However, the Nyquist period of the altimetric data is about 20 days, so estimates of the high-frequency spectral slope are very uncertain. More recent work has found ω^{-2} spectral slopes for velocity in extratropical regions but shallower slopes in the tropics (Scharffenberg and Stammer 2010).

Figure 2 shows observed frequency spectra for the same locations discussed above: 35°N, 168°E and 35°N, 222°E. Both locations exhibit a low-frequency plateau at periods longer than 300 days, appear to approach an ω^{-2} power law near 100 days, but quickly flatten in the high-frequency tails. The frequency spectrum from AVISO gridded altimetry, linearly interpolated along the satellite track, is also shown (Fig. 2). The spectrum from AVISO gridded altimetry is steeper than from ungridded altimetry at periods shorter than about 110 days.

b. Moored kinetic energy

Frequency spectra of velocity and vertical displacement from moorings are generally consistent with an ω^{-2} slope for periods shorter than 30 days in many regions (Ferrari and Wunsch 2010). Figure 3 shows observed kinetic energy spectra from moored current meters at several locations and depths in the North Pacific. Locations are 14°N, 230°E; 28°N, 208°E; 32°N, 232°E; and 39°N, 232°E. Though moorings may be blown over by strong currents, leading to measurements at varying depth, no correction for this effect has been made. All spectra are normalized by the total variance so that the shapes of the spectra can be easily compared.

Overall, a low-frequency plateau transitioning to a high-frequency ω^{-2} power law exists in all the results. However, near 100-day periods, the mooring spectra are flatter than similar spectra from altimetry (e.g., Stammer 1997). Strong regional- and depth-dependent differences are seen. For example, the spectral slope tends to become steeper with depth at the 28°N mooring. Also, the frequency of the transition from the low-frequency plateau to a high-frequency power law increases with depth at the 39°N mooring.

c. Moored temperature

Figure 4 shows observed temperature spectra from the moored instruments shown in Fig. 3. Temperature frequency spectra have a shape generally similar to those for kinetic energy. In general, the frequency spectra can again be described as a low-frequency plateau transitioning to a high-frequency ω^{-2} power law.

The observation that frequency spectra of kinetic energy and temperature have roughly the same shape puts an important constraint on the spectrum model. For some functional forms, the characteristic functions for the dynamical model, (9) and (14), would predict different spectra for energy and temperature. For example, suppose $\Phi_\psi \sim (k^2L^2 + l^2L^2 + \omega^2T^2 + 1)^{-\alpha}$, where L and T are characteristic length and time scales, respectively. After multiplying by the appropriate characteristic function and integrating over k and l, the dynamical model predicts high-frequency spectral slopes $\omega^{4-2\alpha}$ for velocity but $\omega^{2-2\alpha}$ for temperature. In contrast, if $\Phi_\psi \sim (k^2L^2 + l^2L^2 + 1)^{-\alpha}\omega^{-2}$, the dynamical model predicts frequency spectral slopes ω^{-2} for both velocity and temperature. The first functional form is inconsistent with observations. This suggests a separable form for the spectrum, at least in the frequency and wavenumber range where the spectrum follows an approximate power law. However, we have already seen that westward motions dominate (Fig. 1), ruling out the possibility of a completely separable spectrum.

d. Shipboard velocity

Wavenumber spectra of kinetic energy are available from both towed and shipboard acoustic Doppler current profiler (ADCP) instruments, with the latter being more common. Shipboard measurements in the Gulf Stream show a k^{-3} spectral slope for kinetic energy, implying k^{-5} in SSH for balanced motions (Wang et al. 2010). In the central North Pacific (25°–35°N, 140°W), spectral slopes from shipboard ADCP are close to k^{-2} for velocity, implying k^{-4} for SSH (J. Callies 2012, personal communication). Both of the in situ spectral slope estimates are steeper than the altimeter-derived estimates in their respective regions (Xu and Fu 2012), casting doubt on spectral slopes estimated from altimetry at these wavenumbers. However, the in situ estimates may include a significant contribution from ageostrophic motions, complicating the interpretation.

The spectrum of velocity at 100 m from a 1000-km meridional transect taken over 5 days as part of the World Ocean Circulation Experiment (WOCE) section P14N (20°–30°N, 180°E; Roden 2005) is shown in Fig. 5.

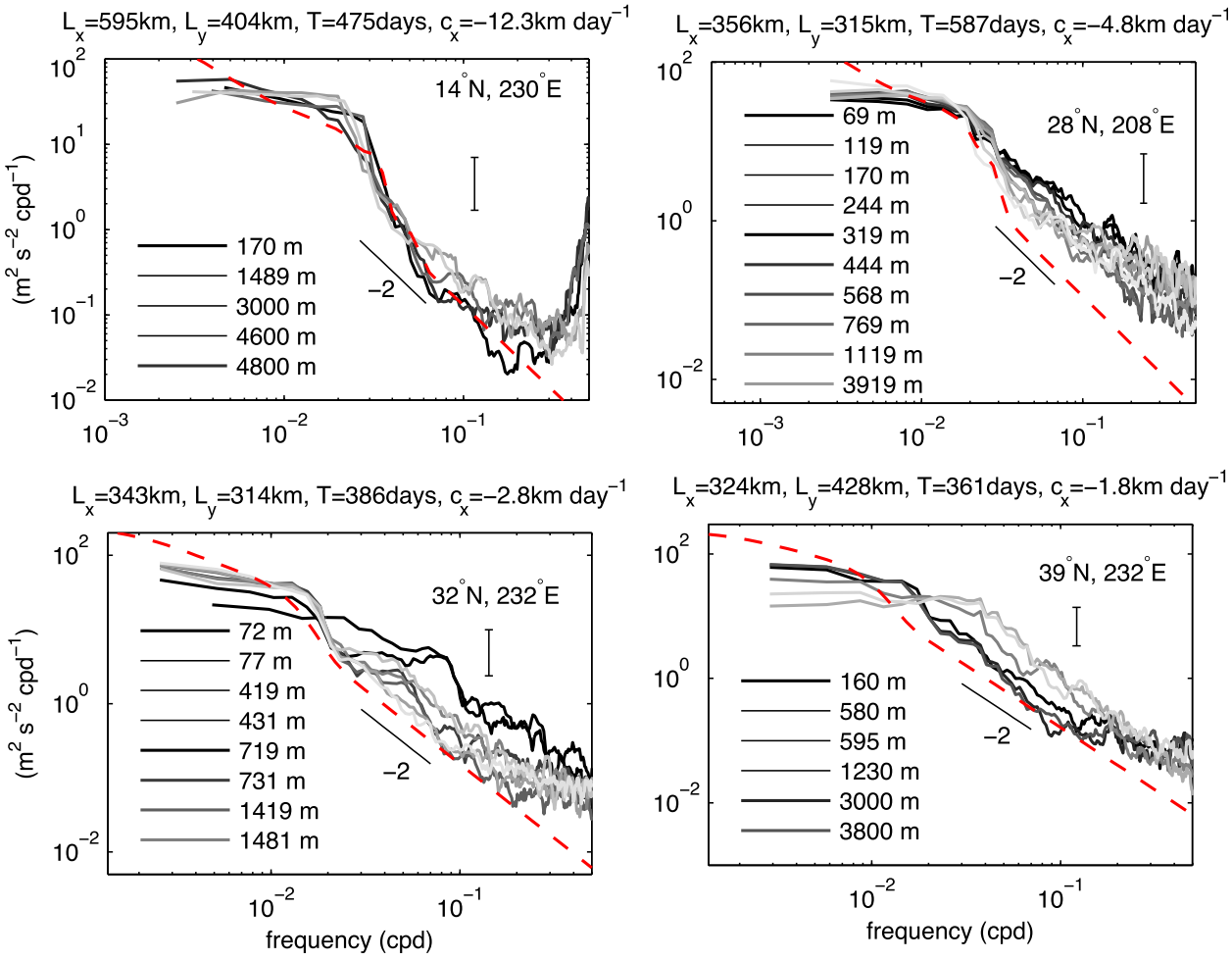

FIG. 3. Observed (solid) and modeled (red dashed, discussed in section 4) frequency spectra of kinetic energy from moored instruments. All spectra are normalized by the total variance to compare the shapes. Vertical bars indicate the 95% confidence interval.

Tidal or other ageostrophic motions are not removed from the record. The observed high-wavenumber spectral slope is close to k^{-2}, implying k^{-4} for SSH.

Taken together, in situ, altimetric, and modeling results are consistent with wavenumber spectral slopes in the subtropical North Pacific of -4 ± 1, with in situ results suggesting slightly steeper slopes than altimetric results.

e. *Vertical structure*

Most of what is known from observations about the vertical structure of variability is based on Wunsch (1997, 1999). Those results support the inference that in the vertical dimension a modal representation is most useful (a contrast with the internal-wave case). The basic inference was that about 50% of the water column kinetic energy is in the barotropic mode, about 40% is in the first baroclinic mode, and the remainder is in higher baroclinic modes and noise. The modes were defined as the basic flat-bottom resting-ocean Rossby-wave modes. However, Wunsch (1997) found evidence of coupling between the modes, such that the total surface kinetic energy was different from the sum of the energy in each mode. Müller and Siedler (1992) computed EOFs from several multiyear moorings in the North Atlantic Ocean. The leading EOF generally had a surface-intensified shape, similar to the first baroclinic mode but with no zero crossing. Decomposition into dynamical modes showed coupling between the barotropic and first baroclinic modes, especially during the most energetic events.

Given the short duration of most current-meter moorings, almost no observational information exists about the vertical structure of currents at periods beyond about a year. Wortham (2013) resorted to GCM results, based on the 1/6° ECCO2 model (Menemenlis et al. 2008), which suggested that the barotropic and first baroclinic modes are strongly coupled, especially at interannual periods.

The general lack of evidence on which to base conclusions about the vertical structure of balanced motions

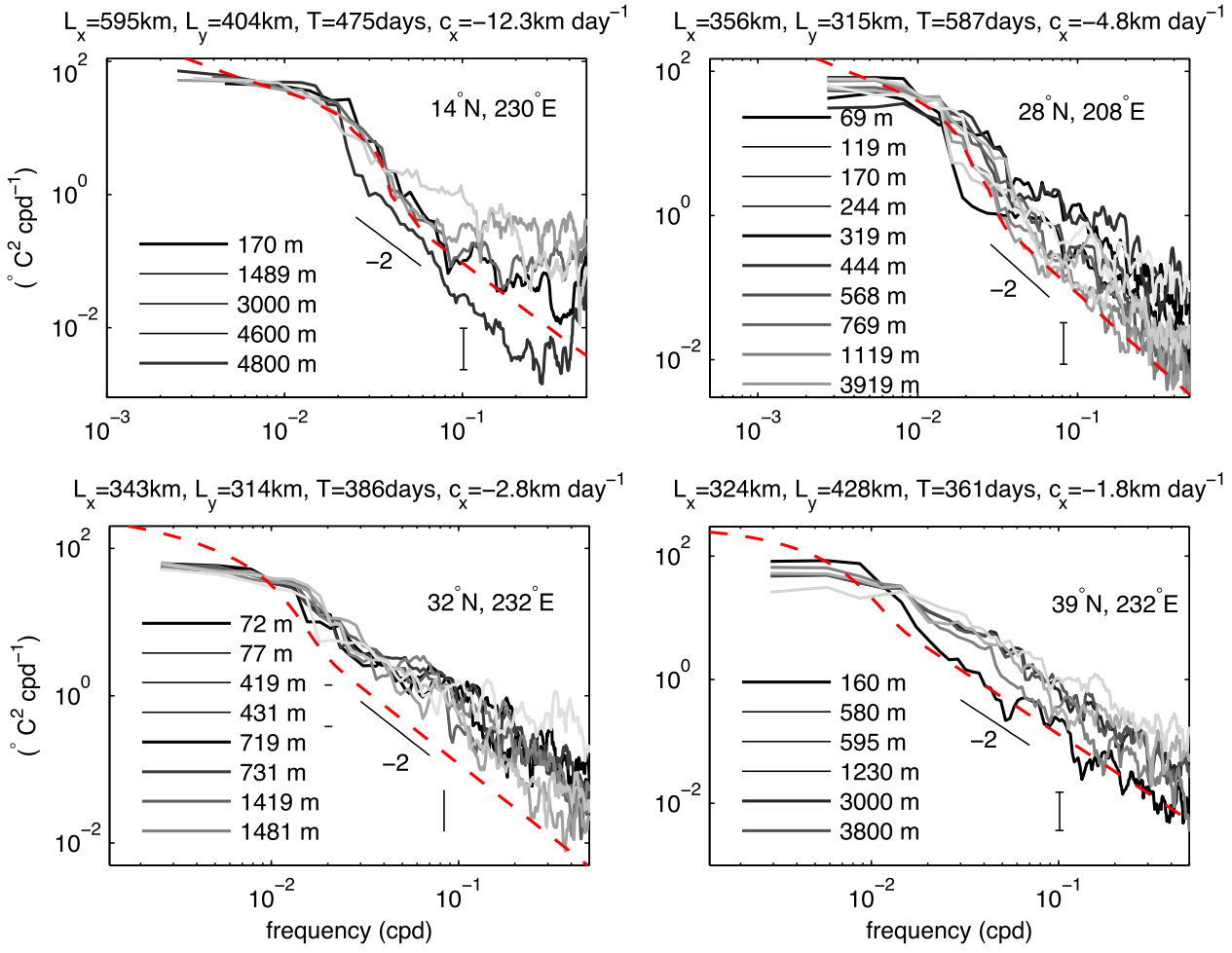

FIG. 4. As in Fig. 3, but for the temperature spectrum.

has been discussed by Wunsch (2009, 2010) and Ferrari and Wunsch (2010). In the absence of further observations, we take the evidence from the ECCO2 GCM (Wortham 2013) as the basis for the spectrum model vertical structure, presented in section 5. The vertical structure of balanced motions, especially at periods longer than a year, deserves further study.

4. Model k–l–ω spectrum

The spectrum model presented as a zero-order approximation by Zang and Wunsch (2001) was universal in shape (only the amplitude changed with location) and separable in frequency and wavenumber. However, important quantities, such as the first moments of the observed spectrum, vary geographically and observations of the nondispersive line are incompatible with a separable form. However, many observations are consistent with a single spectral form with suitable slowly varying parameters.

A quantitatively useful analytical description of the observed spectra is sought, along with some description of its accuracies. For the horizontal wavenumber–frequency spectrum discussed in section 3, the structure is captured by

$$\Phi_\psi(k,l,\omega;\phi,\lambda)=\frac{1}{(k^2L_x^2+l^2L_y^2+1)^\alpha(\omega^2T^2+1)}+\exp\{-[k^2L_x^2+l^2L_y^2+T^2(kc_x+lc_y-\omega)^2]\}, \tag{30}$$

where α, L_x, L_y, T, c_x, and c_y are geographically variable parameters. Equation (30) has two parts. A power law appears in the first term, with parameters L_x, L_y, and T controlling the dominant wavelengths and period of the

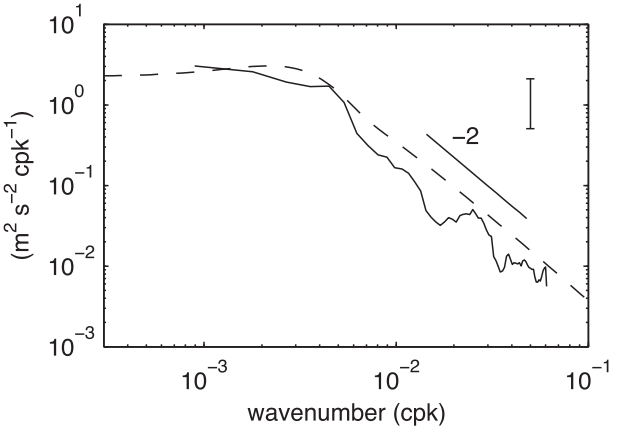

FIG. 5. Observed (solid) and modeled (dashed, discussed in section 4) wavenumber spectra of kinetic energy from shipboard ADCP. The transect spans 20°–30°N at 180° at 100-m depth. The high-wavenumber spectral slope for the model is k^{-2}. The vertical bar indicates the 95% confidence interval.

spectrum, while α sets the high-wavenumber spectral slope. An exponential term enforces the dominance of westward propagation. The exponential term only makes a significant contribution in the range of wavenumber–frequency space corresponding to the nondispersive line. This model is entirely empirical and is judged by the authors to provide a reasonable fit to the wide variety of observations described in section 3. Consistency between the spectrum model and observations will be discussed below. The full spectrum model is illustrated in Fig. 6 as a set of two-dimensional spectra averaged over positive and negative wavenumber half spaces. Figure 7 displays a three-dimensional version.

Integrating (30) over l and ω produces the zonal wavenumber spectrum:

$$\Phi_\psi(k;\phi,\lambda) = \int_{-\infty}^{\infty}\int_0^{\infty} \Phi_\psi(k,l,\omega;\phi,\lambda)\,d\omega\,dl$$

$$= \frac{\pi^{3/2}\Gamma(\alpha-1/2)}{2TL_y\Gamma(\alpha)}(1+k^2L_x^2)^{1/2-\alpha} + \frac{\pi}{2TL_y}e^{-k^2L_x^2}\left[1+\mathrm{erf}\left(\frac{kc_xL_yT}{\sqrt{L_y^2+c_y^2T^2}}\right)\right], \quad (31)$$

where $\mathrm{erf}(z)$ is the error function

$$\mathrm{erf}(z) = \frac{2}{\sqrt{\pi}}\int_0^z e^{-t^2}\,dt, \quad (32)$$

with a similar expression for $\Phi_\psi(l;\,\phi,\,\lambda)$. At a high wavenumber, the first term dominates and approaches a power law in k with slope $1-2\alpha$. Although wavenumber

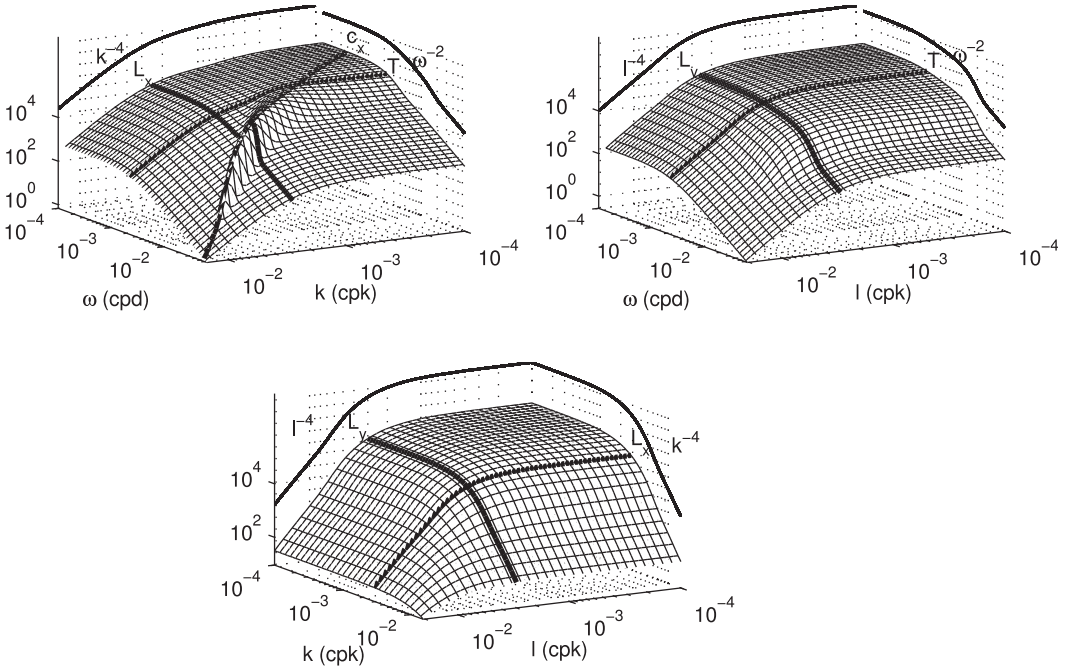

FIG. 6. The spectrum model (30) for SSH near 30°N, 190°E. Two-dimensional spectra (top left) $\Phi_\eta(k,\omega)$, (top right) $\Phi_\eta(l,\omega)$, and (bottom) $\Phi_\eta(l,k)$ are shown. Solid lines indicate the parameters in the model. One-dimensional spectra are projected on a vertical plane, with high-frequency/wavenumber power laws labeled. The nondispersive line, with phase speed c_x, is most prominent in the k–ω spectrum. Because of the difficulty of plotting positive and negative wavenumbers together on a logarithmic scale, we show the average of the positive and negative wavenumber half spaces.

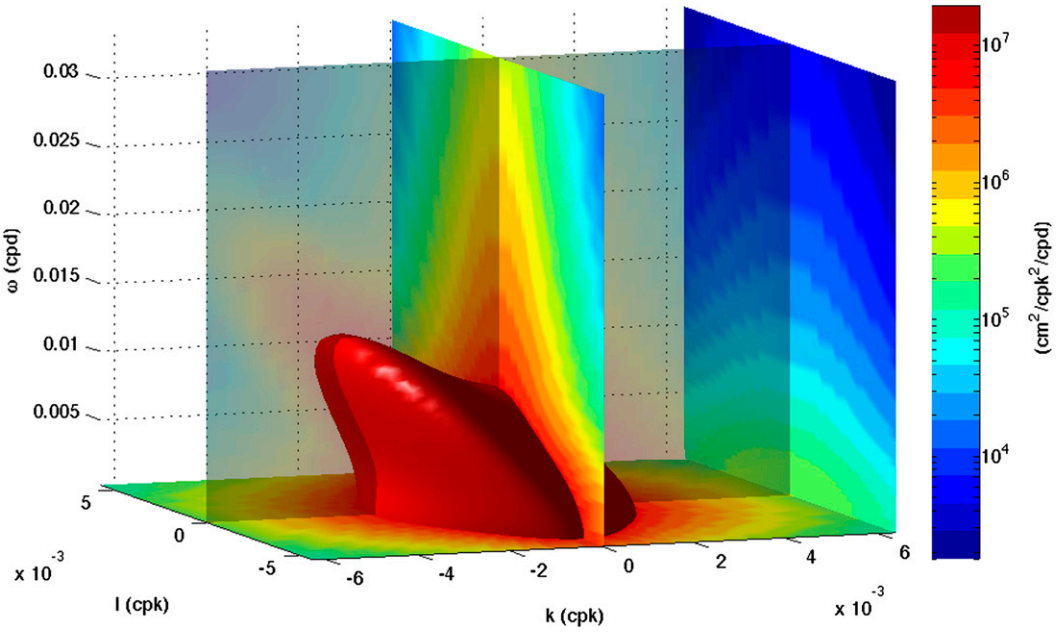

FIG. 7. A 3D representation of the spectrum model (30) for SSH near 30°N, 190°E. The red isosurface illustrates the nondispersive line. Slices through the planes $\omega = 0$, $l = 0$, $k = 0$, and $k = 6 \times 10^{-3}$ cycles per kilometer (cpk) are shown.

spectral slopes from altimetry vary geographically (Xu and Fu 2012), considerable uncertainty exists in the actual values, as discussed in section 3. In light of this uncertainty, a constant $\alpha = 5/2$ is used, to be updated when more reliable observations become available. The resulting one-dimensional wavenumber spectral slope is k^{-4} for SSH and k^{-2} for kinetic energy.

Integrating (30) over k and l produces the frequency spectrum:

$$\Phi_\psi(\omega;\phi,\lambda) = \int_{-\infty}^{\infty}\int_{-\infty}^{\infty} \Phi_\psi(k,l,\omega;\phi,\lambda)\,dk\,dl$$

$$= \frac{\pi}{(\alpha-1)L_xL_y}(1+\omega^2T^2)^{-1} + \frac{\pi}{\sqrt{D}}\exp(-L_x^2L_y^2T^2\omega^2/D), \tag{33}$$

where

$$D = c_x^2L_y^2T^2 + L_x^2L_y^2 + c_y^2L_x^2T^2. \tag{34}$$

At high frequency, the first term dominates and approaches an ω^{-2} power law. This spectral slope applies to both SSH and kinetic energy.

The most important parameters in the spectrum model (30) are L_x, L_y, and T, which set the dominant wavelengths and periods. These parameters are chosen such that the first moment of the spectrum model matches inferences from the AVISO product (Fig. 1). From (28) with (31) (and the equivalent relations for l), the first moment of the wavenumber spectrum is

$$\langle k^1\rangle = \frac{(\alpha-1)[\sqrt{\pi}\Gamma(\alpha-3/2)+\Gamma(\alpha)]}{L_x\sqrt{\pi}(\alpha+\sqrt{\pi}-1)\Gamma(\alpha)} \quad \text{and}$$

$$\langle l^1\rangle = \frac{(\alpha-1)[\sqrt{\pi}\Gamma(\alpha-3/2)+\Gamma(\alpha)]}{L_y\sqrt{\pi}(\alpha+\sqrt{\pi}-1)\Gamma(\alpha)}. \tag{35}$$

Given $\langle k^1\rangle$ and $\langle l^1\rangle$ estimated from the AVISO product (Fig. 1), L_x and L_y are calculated from (35) at each location.

The first moment of the frequency spectrum of SSH depends, unfortunately, on the limits of integration. Integrating (27) with (33) to an upper frequency limit $\omega_{\max}$,

$$\langle\omega^1\rangle = \frac{\pi(\alpha-1)\sqrt{D}[1-\exp(-\omega_{\max}^2L_x^2L_y^2T^2/D)] + \pi L_xL_y\ln(1+\omega_{\max}^2T^2)}{L_xL_yT[2\pi\arctan(\omega_{\max}T) + \pi^{3/2}(\alpha-1)\operatorname{erf}(\omega_{\max}L_xL_yT/\sqrt{D})]}. \tag{36}$$

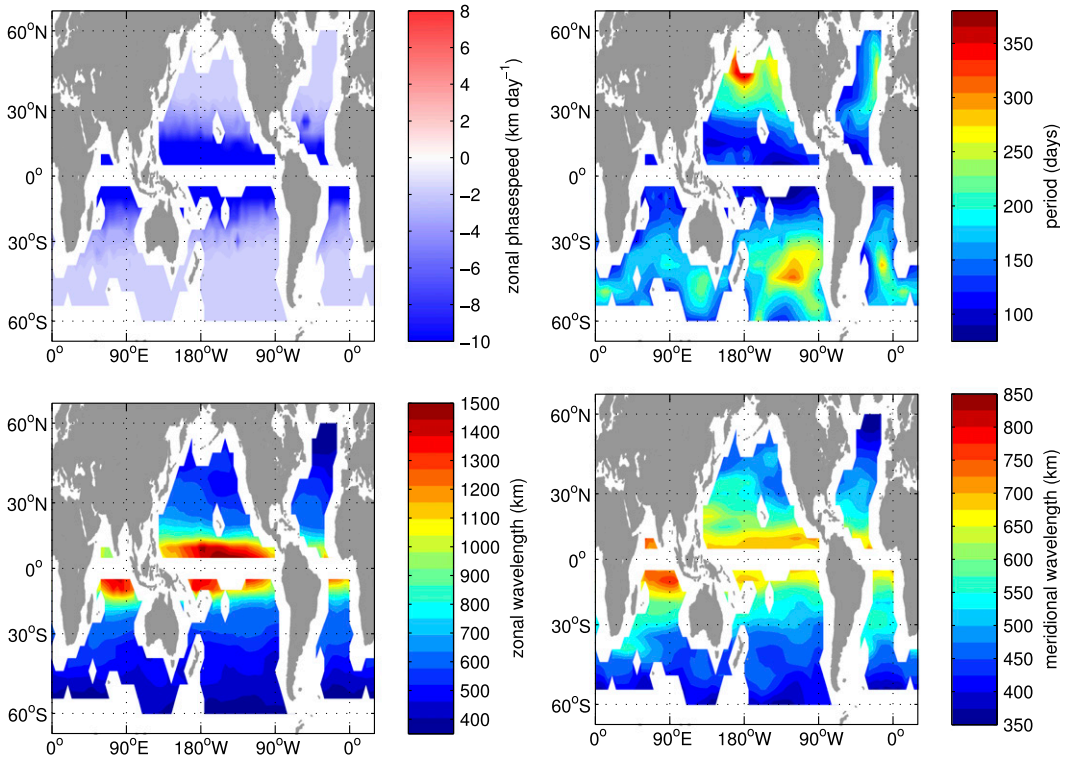

FIG. 8. Global characteristics of the spectrum model (30). (top left) Dominant zonal phase speed, (top right) period, (bottom left) zonal wavelength, and (bottom right) meridional wavelength based on the first moment of the associated one-dimensional spectra.

Given L_x, L_y, and $\langle\omega^1\rangle$ estimated from the AVISO product (Fig. 1), (36) can be solved numerically for T at each location. Here, we use $\omega_{\max} = 1\ (14\,\text{days})^{-1}$, corresponding to the Nyquist frequency of the AVISO product.

The parameters c_x and c_y control the dominant zonal and meridional phase speeds in the spectrum model. The term $c_x = \omega/k$ is the result of the eigenvalue problem for the vertical structure [e.g., (3)]. In practice, the phase speed obtained from the modified eigenvalue problem discussed in section 5 is used instead. Given the very weak asymmetry between northward and southward motions, we set $c_y = 0$ everywhere.

The spectrum model (30) is intended to approximate the observed spectrum for periods between the inertial period and about 10 yr and wavelengths between 100 and 10 000 km. These limits are primarily set by the duration and spatial resolution of the altimetric product that was used to inform the spectrum model (Chelton et al. 2011). The important question of the behavior of the frequency spectrum as ω approaches zero is beyond the scope of this work, but has been discussed elsewhere (Wunsch 2010, and references therein). As $\omega \to 0$, the spectrum model here becomes white in frequency with consequences for trend determination. In the remainder of this section, the predictions of (30) are compared with various observed spectra.

a. Global patterns

The spectrum model (30) is spatially variable, resulting in realistic patterns of dominant phase speed, period, and wavelength (Fig. 8), with values comparable to Fig. 1. The main difference is between phase speeds from AVISO and the spectrum model; the eigenvalue problem used to set c_x in the spectrum model does not permit eastward phase speeds.

b. Alongtrack altimetry

Figure 2 compares wavenumber spectra of SSH from the spectrum model and altimetry. The spectrum model is normalized such that it has the same total variance as the observed one. In both regions, the model captures the general shape of the observed spectrum at wavelengths larger than 200 km. In particular, the transition from plateau to power law occurs at the same wavelength in the spectrum model as in the altimetric spectrum. The model has a constant high-wavenumber spectral slope of k^{-4} for SSH and does not agree with the altimetric spectra for scales smaller than about 200 km,

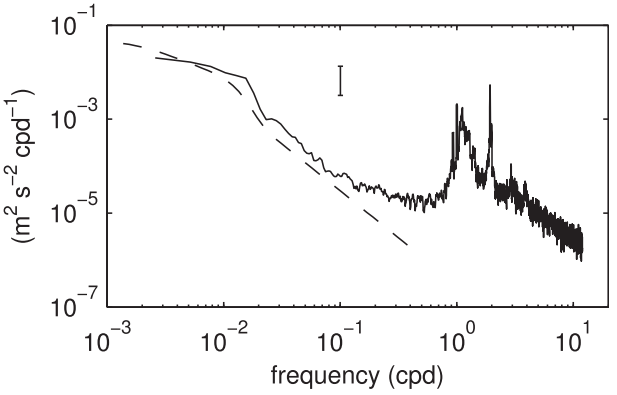

FIG. 9. Observed (solid) and modeled (dashed) frequency spectra of kinetic energy from moored instruments at 32°N, 232°E, 1481 m deep, as in Fig. 3, but now expanded to show the internal-wave regime. The spectral peaks are at the inertial and M_2 tidal frequencies.

where the observations are contaminated by measurement noise (Xu and Fu 2012).

Figure 2 also shows modeled frequency spectra for the same locations. Again, the spectrum model transitions from plateau to power law at the same frequency as the altimetric spectrum, and the ω^{-2} power law is a reasonable fit for periods longer than about 60 days. The frequency of the transition is set by the parameter T. At shorter periods, the spectrum from alongtrack altimetry flattens, but the spectrum model follows the spectrum from AVISO.

c. Moored kinetic energy

Figure 3 shows normalized modeled kinetic energy spectra at several locations and depths in the North Pacific. Overall, the spectrum model follows the observed values and captures the transition from plateau to ω^{-2} power law and, over most of the frequency range, is within the estimated uncertainty of the observed spectra. Although Fig. 3 suggests that the spectral shape changes with depth, these changes are not statistically significant given the available data and are not reflected in (30).

As ω approaches $f/(2\pi)$ from below, the observed spectrum (Fig. 9) transitions smoothly into the internal-wave regime at frequencies not modeled here. The transition regime between the present model and the Garrett–Munk spectrum, plus tidal and inertial peaks, remains to be properly represented, an effort not undertaken here.

d. Moored temperature

Figure 4 shows normalized temperature spectra from the moored instruments shown in Fig. 3. Again, for most instruments, the spectrum model follows the observed spectra within the estimated uncertainty of the latter.

e. Shipboard velocity

The model wavenumber spectrum of kinetic energy is shown in Fig. 5. At this location, the spectrum model amplitude was lower than that observed by a factor of 2 and is normalized to have the same total variance as the observations so that the spectral shape can be compared. The model k^{-2} spectral slope is close to that observed, and the spectrum model is within the estimated uncertainty of the observed spectrum at all wavelengths.

5. Model vertical structure

The vertical structure of the spectrum model proposed by Zang and Wunsch (2001) was largely based on the observations of Wunsch (1997). They used the representation of (3) under BTT boundary conditions with mode partition $E(0) = 1$, $E(1) = 1$, $E(2) = ½$, and $E(n) = 0$ for $n \geq 3$ in (20). While this recipe works in some locations (Zang and Wunsch 2001), it has a strong tendency to overestimate kinetic energy in the abyss and underestimate kinetic energy near the surface. That is, kinetic energy is more surface intensified than their vertical structure predicted. Wortham (2013) suggests that such a systematic misfit to the observed kinetic energy profile is indicative of coupling between the barotropic and baroclinic modes.

Several dynamical processes have been proposed to explain the surface intensification of kinetic energy. These include the impact of mean flow (Keller and Veronis 1969; Killworth et al. 1997; Dewar 1998; de Szoeke and Chelton 1999; Killworth and Blundell 2004, 2005), large-scale sloping topography (Killworth and Blundell 1999), small-scale rough topography (Rhines and Bretherton 1973; Samelson 1992; Bobrovich and Reznik 1999; Tailleux and McWilliams 2001), surface forcing by Ekman pumping (Frankignoul and Müller 1979a,b; Müller and Frankignoul 1981; Killworth and Blundell 2007), SQG dynamics (Lapeyre and Klein 2006; LaCasce 2012), and nonlinearity (McWilliams and Flierl 1979; Vanneste 2003; Chelton et al. 2007, 2011). See Wortham (2013) and references therein for a more complete discussion. We focus on the roles of mean flow and rough topography because they predict the observed vertical structure, while recognizing that other dynamics may be important too.

Samelson (1992) found that rough topography produced surface-intensified Rossby waves in a two-layer model, and Bobrovich and Reznik (1999) provided an analytical description of the effect in a constant stratification. The latter showed that rough topography reduces

the wave amplitude near the bottom, though this analytical theory is difficult to apply for realistic stratification. Tailleux and McWilliams (2001) have presented a simple approximation of the impact of topography through their bottom pressure decoupling (BPD) theory. Essentially, the BPD formulation replaces the standard bottom boundary condition, $dF/dz = 0$, with $F(z) = 0$ at $z = -H$. Aoki et al. (2009) showed that this BPD theory and mean flow both improved the representation of vertical structure in a GCM.

Consider the quasigeostrophic vorticity equation, linearized about the local mean state $\mathbf{U} = U(z)\mathbf{i} + V(z)\mathbf{j}$ (Aoki et al. 2009):

$$\left(\frac{\partial}{\partial t} + U\frac{\partial}{\partial x} + V\frac{\partial}{\partial y}\right)\left[\nabla^2\psi + \frac{\partial}{\partial z}\left(\frac{f_0^2}{N^2}\frac{\partial\psi}{\partial z}\right)\right] - \frac{\partial}{\partial z}\left(\frac{f_0^2}{N^2}\frac{\partial V}{\partial z}\right)\frac{\partial\psi}{\partial y} + \left[\beta - \frac{\partial}{\partial z}\left(\frac{f_0^2}{N^2}\frac{\partial U}{\partial z}\right)\right]\frac{\partial\psi}{\partial x} = 0, \quad -H < z < 0. \tag{37}$$

Imposing wave solutions in the form $\psi(x, y, z, t) = F(z)e^{-i2\pi(kx+ly-\omega t)}$ in (37), the vertical structure satisfies

$$(\mathbf{K}\cdot\mathbf{U} - \omega)\left[\frac{\partial}{\partial z}\left(\frac{f_0^2}{N^2}\frac{\partial}{\partial z}\right) - K^2\right]F(z) = \left\{l\frac{\partial}{\partial z}\left(\frac{f_0^2}{N^2}\frac{\partial V}{\partial z}\right) - k\left[\beta - \frac{\partial}{\partial z}\left(\frac{f_0^2}{N^2}\frac{\partial U}{\partial z}\right)\right]\right\}F(z), \tag{38}$$

where $\mathbf{K} = (k, l)$ and $K = \sqrt{k^2 + l^2}$. Given the mean flow $\mathbf{U}$, stratification N^2, and suitable boundary conditions, (40) forms an eigenvalue problem that can be solved for the eigenmodes $F_n(z)$ and eigenvalues ω_n ($n = 0, 1, 2, \ldots$).

Following the formulation of Aoki et al. (2009), including the effects of mean flow and BPD, the vertical modes are the eigenmodes of (40) subject to the boundary conditions

$$dF/dZ = 0 \quad \text{at} \quad z = 0 \quad \text{and} \tag{39}$$

$$F = 0 \quad \text{at} \quad z = -H. \tag{40}$$

We use $l = 0$ and $k = 1/(100L_d)$, effectively in the long-wave limit, where L_d is the BTT first-baroclinic-mode deformation radius. Mean flow $\mathbf{U}$, salinity S, and potential temperature θ are taken from the Ocean Comprehensible Atlas (OCCA; Forget 2010), and stratification is computed using a neutral density calculation (Chelton et al. 1998).

Comparison with vertical profiles of EKE and temperature variation at the four mooring sites shown in Figs. 3 and 4 produced a reasonable fit with the mode coefficients $E(0) = ½$, $E(1) = 1$, $E(2) = ¼$, $E(3) = 1/10$, and $E(n) = 0$ for $n \geq 4$. These coefficients are then used globally. The coefficients $E(n)$ used here are preliminary, and the representation of the vertical structure in the spectrum model deserves further study. The resulting spectrum model vertical structure is discussed below.

A possible significant shortcoming of the representation in (20) is the assumption that the vertical structure is independent of period/wavelength. In almost all extensions (e.g., Tailleux and McWilliams 2001; Killworth and Blundell 2004; Lapeyre and Klein 2006), vertical mode structure depends on wavelength. With existing observational technologies, the period/wavelength dependence of the vertical structure will be very difficult to determine.

EKE(z) *and* $\sigma_\theta(z)$ *profiles*

The appendix describes by example how to compute various quantities from the spectrum model. Here some summary comparisons with other observations are made. Figure 10 compares the vertical profile of kinetic energy for the spectrum model with subinertial kinetic energy from the set of current meters discussed in section 3b. Subinertial kinetic energy is estimated by integrating its spectrum over frequencies below 1/5 cpd for each instrument, and a similar estimate is made from the model. For most instruments, the model kinetic energy agrees with the observed to within a factor of 2, indicated by gray shading in the figure, and often better. The main exception is near 1000 m at 28°N, where the model overestimates the observed kinetic energy by a factor of 3.

Figure 11 compares the vertical profile of temperature standard deviation σ_θ for the spectrum model with observations from moored temperature sensors. The predicted temperature standard deviation is within a factor of 2 of the observations in almost all cases, as indicated by gray shading in the figure. An example of the calculation of temperature standard deviation is reproduced in the appendix.

For a further evaluation of the spectrum model, we expand the analysis to the large number of moored current-meter and temperature sensors collected in the Global Multi-Archive Current Meter Database (CMD; Scott et al. 2010). We found 4112 current-meter records, with a duration of at least 180 days, moored in water deeper than 1000 m. From this set, we excluded records with quality control flags set in the original archive, records with less than 50% data coverage, and instruments within 5° of the equator or 2.5° of land. These criteria resulted in 2179 current-meter records and 1948 temperature

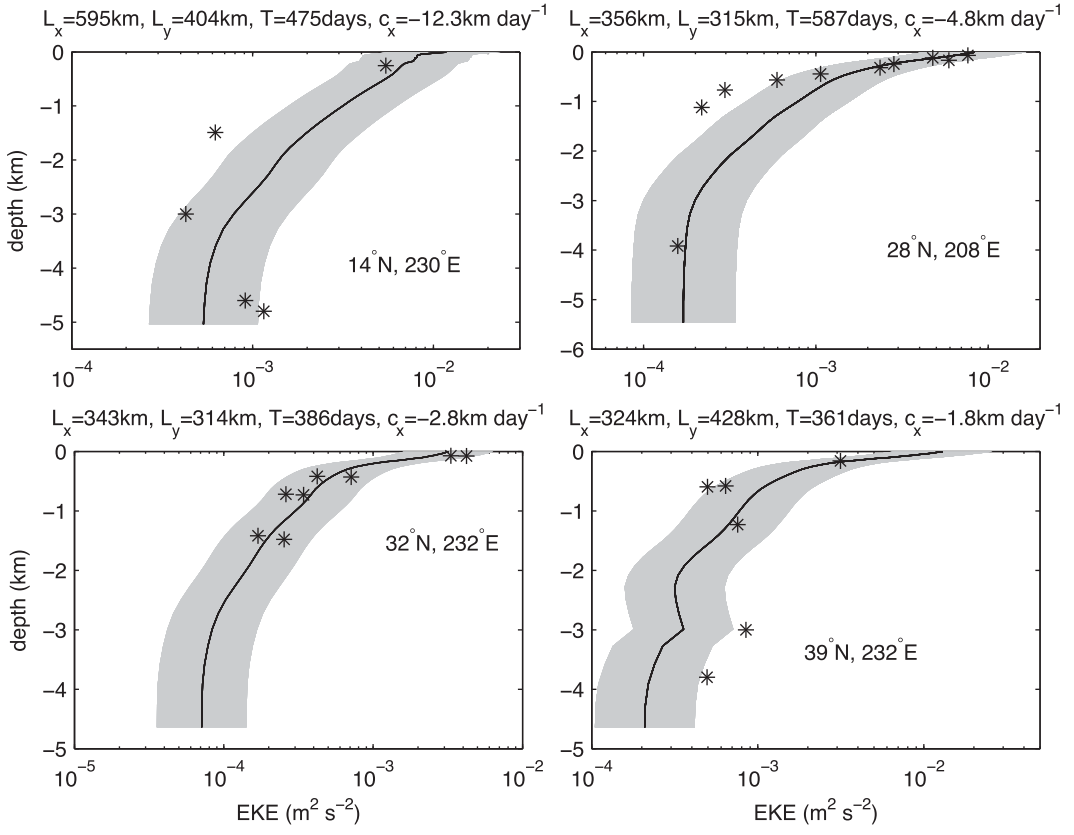

FIG. 10. Observed (asterisks) and modeled (solid line) kinetic energy as a function of depth from moored instruments. Gray shading indicates EKE within a factor of 2 of the spectrum model prediction. Moorings are the same as those shown in Figs. 3 and 4.

records included in the analysis. The locations of these instruments are mapped in Fig. 12.

The sampling frequencies for the records analyzed vary from 5 min to 1 day. To produce homogeneous records for comparison with the spectrum model, all records are reduced to 5-day moving averages. When there are missing data in a 5-day window, the average is computed as long as there are at least 2.5 days of good data within the window; otherwise, the time period is flagged as missing and no temporal interpolation is made. For each 5-day-averaged time series, we compute the EKE and temperature standard deviation σ_θ. For each record, EKE and σ_θ are computed from the spectrum model at the instrument location and depth.

Scatterplots compare the EKE and σ_θ from the spectrum model with the CMD records (Fig. 13). If there were perfect agreement between the spectrum model and the CMD records, all points would fall along the 45° line. For EKE, there is strong correlation between the spectrum model and observed values (Pearson correlation coefficient $r = 0.85$). Conspicuous in the EKE scatterplot is a cluster of points well below the 45° line, with the spectrum model underestimating the observed EKE. At these points the spectrum model vertical structure for EKE is very surface intensified. This surface intensification is caused by the local mean flow $\mathbf{U}$ in (40). Strong, presumably unrealistic surface intensification in the spectrum model occurred in about 50 cases. For σ_θ, the correlation is weaker ($r = 0.77$) and the spectrum model is biased high. Both correlations are highly statistically significant ($P < 10^{-4}$).

Biases in the spectrum model are revealed by examining the following statistic, similar to that used by Scott et al. (2010):

$$D_{\mathrm{EKE}} = \frac{\mathrm{EKE}_{\mathrm{CMD}} - \mathrm{EKE}_{\mathrm{MOD}}}{\mathrm{EKE}_{\mathrm{CMD}} + \mathrm{EKE}_{\mathrm{MOD}}} \quad \text{and} \tag{41}$$

$$D_{\sigma_\theta} = \frac{\sigma_{\theta,\mathrm{CMD}} - \sigma_{\theta,\mathrm{MOD}}}{\sigma_{\theta,\mathrm{CMD}} + \sigma_{\theta,\mathrm{MOD}}}, \tag{42}$$

where subscripts CMD and MOD indicate values from the observations and the spectrum model, respectively. This statistic maps the discrepancy onto the interval

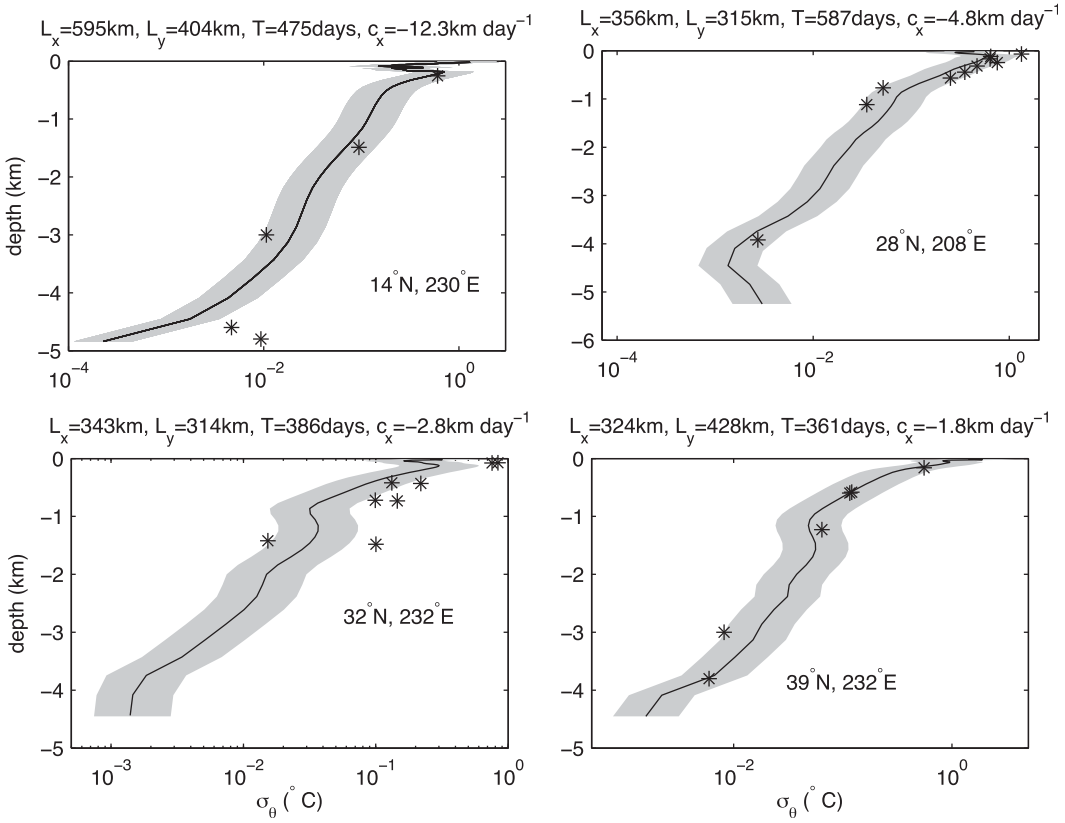

FIG. 11. As in Fig. 10, but showing the vertical structure of temperature variance. Gray shading indicates σ_θ within a factor of 2 of the spectrum model prediction.

[−1, 1]. For perfect agreement between the spectrum model and observations, D_{EKE} and D_{σ_θ} would be distributed like the Dirac delta function.

Figure 14 shows histograms of D_{EKE} and D_{σ_θ}, grouped by instrument depth. Depth bins are 0–700, 700–3000, and below 3000 m. The depth bins are selected to give roughly equal numbers of instruments in each bin. Overall, EKE from the spectrum model is slightly stronger than from the CMD, with the strongest bias in the 700–3000-m bin. The distribution of D_{σ_θ} reveals the depth dependence of the spectrum model bias. Above 700 m, the spectrum model σ_θ tends to be smaller than observed, while between 700 and 3000 m, the spectrum model σ_θ tends to be larger. Below 3000 m, the spectrum model has a strong bias toward high σ_θ. Median values for D_{EKE} and D_{σ_θ} in each depth bin represent the spectrum model bias (Table 1).

6. Applications

Many potential applications, both theoretical and practical, exist for the spectrum model. At the core of the theoretical applications lies the need to explain why it takes on the characteristics it does, including power laws, dispersion curves, and modal coupling. Although some of these have been touched upon in the discussion of the construction of the model, these and similar questions are not pursued further here. The model can also be used to predict spectral energy and enstrophy

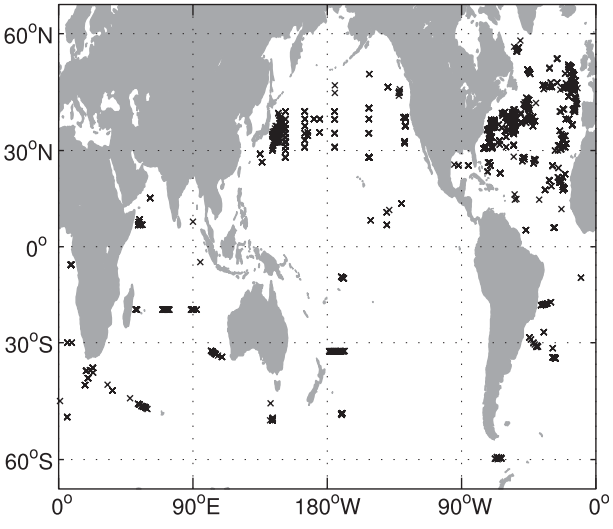

FIG. 12. Locations of current-meter mooring sites.

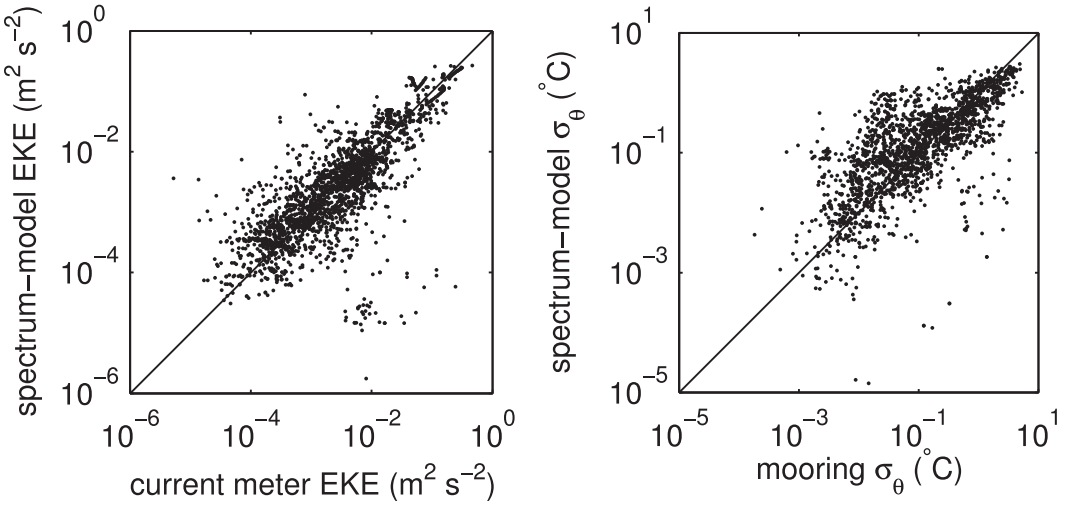

FIG. 13. Scatterplots of (left) EKE and (right) σ_θ from the spectrum model and CMD instruments.

fluxes, as in Scott and Wang (2005) and Arbic et al. (2012). Finally, the spectrum model can be used to estimate isopycnal eddy diffusivities. Following Taylor (1921), diffusivity due to mesoscale eddies can be expressed in terms of the Lagrangian velocity autocorrelation function that, in turn, can be estimated from the spectrum model (Davis 1982; Zang 2000).

The spectral representation is also useful in discussions of space–time sampling requirements for a variety of physical parameters, including the variability of volume flux across a latitude line or heat content, determination of the accuracy of estimated values, and the significance of any observed purported trends. As one illustration of this type of application, Wunsch (2008) used estimates of eddy variability to show that time series of meridional transport calculated from a pair of moorings spanning the North Atlantic will exhibit stochastic fluctuations with multiyear time scales. Such stochastic fluctuations complicate the task of identifying secular trends in the ocean circulation related to climate change. Equation (30) can also be used to predict unobserved spectra, such as for the wavenumbers of vertical displacement.

Many practical applications of the spectrum model rely on estimates of space and time correlation functions, given by (23). The one-dimensional correlation functions of temperature as a function of zonal, meridional, and temporal separation are shown in Fig. 15. At 30°N, 190°E, the correlations show approximately exponential decay, with *e*-folding wavelength of 125 km for zonal separation, 110 km for meridional separation, and 40 days for temporal separation.

The correlation function is useful, for example, in objective mapping of satellite and in situ data. In this context, the spectrum model provides an estimate of the signal covariance. In objective mapping, the goal is to estimate the value of a field χ at a general point

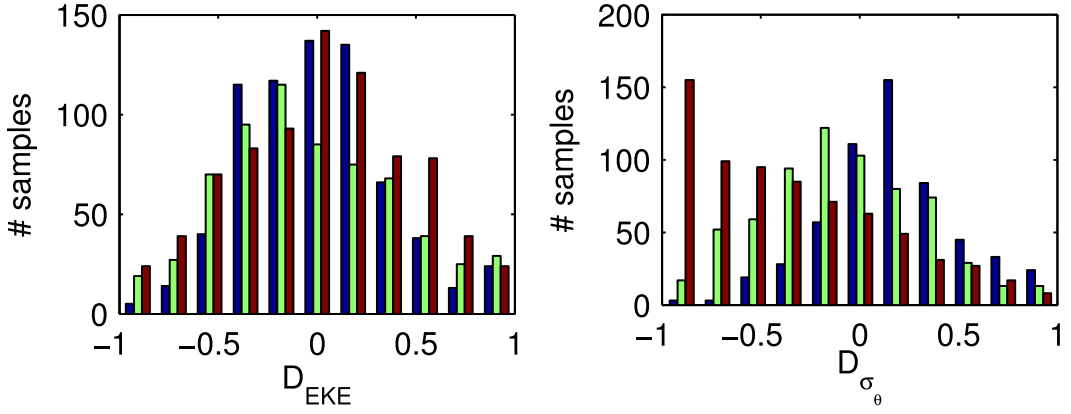

FIG. 14. The distribution of (left) D_{EKE} and (right) D_{σ_θ} for three depth ranges: 0–700 (blue), 700–3000 (green), and below 3000 (red) m.

TABLE 1. Statistics for comparison of the spectrum model and the CMD. Instrument locations are shown in Fig. 12. Median D_χ values represent the bias of the spectrum model for EKE or σ_θ within each depth bin.

Quantity	EKE	σ_θ
No. of instruments	2179	1948
Correlation	0.85	0.77
Median D_χ, < 700 m	−0.01	0.16
Median D_χ, 700–3000 m	−0.10	−0.11
Median D_χ, > 3000 m	0.01	−0.45

$\tilde{r}$ given a set of measurements y at positions r_i. While simple linear interpolation is often used, more general methods (e.g., Bretherton et al. 1976; Wunsch 2006, his section 3.2) make use of covariances within the signal and noise, which can be estimated from the spectrum model.

Using (26), we plot the meridional velocity coherence at 30°N, 190°E for meridional separations between 0 and 200 km (Fig. 16). Since the spectral shape is independent of depth, the predicted coherence is the same at all depths. As expected from the autocorrelation function, there is little coherence for separation beyond about 100 km. An example coherence calculation is reproduced in the appendix.

Finally, the model is applicable to observing system design and trend detection. In this context, the spectrum provides the noise covariance. One can estimate, for example, the number of deep Argo floats needed to detect temperature trends in the abyssal ocean over a given time period. This and other applications are left for future study.

7. Discussion

A strawman empirical model of the four-dimensional spectral density of balanced motions (periods longer than about 20 days but shorter than a decade and wavelengths from about 100 km to several thousands of kilometers) is proposed. The model is based on a variety of observations, including satellite altimetry, moored temperature and current meters, and shipboard velocity measurements. A model of the spectrum of the geostrophic streamfunction is presented, and compared with observations assuming simple geostrophic dynamics. However, many regions of the ocean have peculiar dynamics where the model is inaccurate. In particular, no attempt is made to match observations in the near-surface mixed layer, the core of western boundary currents, the Antarctic Circumpolar Current, within about 5° of the equator, or poleward of 50°.

For the horizontal wavenumber–frequency portion of the spectrum, an implicit two-scale approximation is made; a locally uniform spectrum is modulated by slowly varying geographical parameters L_x, L_y, T, and c_x. These parameters determine the dominant space and time scales of the spectrum, as well as a dominant propagation direction. In this way, a single analytical expression (30) represents the shape of the spectrum over much of the ocean. A typical spectrum is shown in Fig. 6.

The amplitude of the spectrum model is set to match altimetric observations of the surface eddy kinetic energy. The depth dependence is expressed in terms of Rossby wave vertical modes, modified to account for the effects of mean flow and rough topography (Tailleux and McWilliams 2001; Aoki et al. 2009). Including these two effects greatly improves the agreement with observations over the conventional flat-bottom, resting-ocean theory that does not capture the observed surface intensification of kinetic energy. The possibility that other dynamical processes (e.g., the generation of strongly surface-intensified eddies by baroclinic instability) contribute to the observed vertical structure is not excluded.

Explanation of the energy levels and spectral shape is not the goal here. We can, however, speculate to a

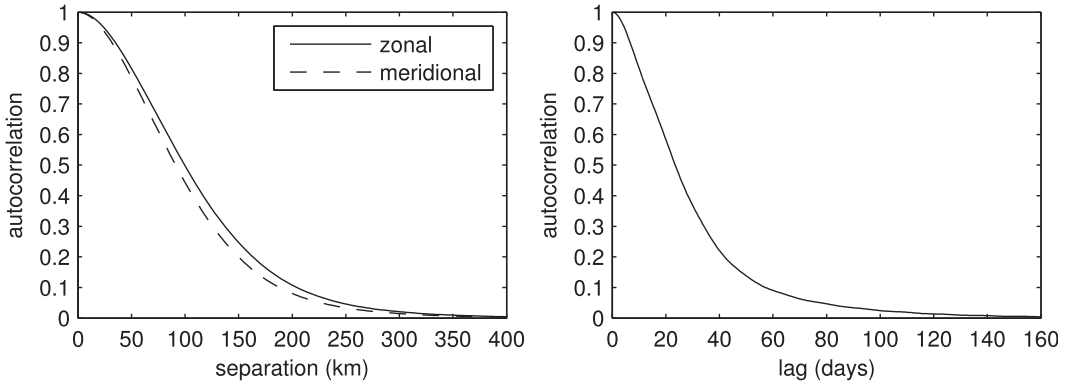

FIG. 15. Autocorrelation function for temperature as a function of (left) spatial and (right) temporal separation based on the spectrum model at 30°N, 190°E.

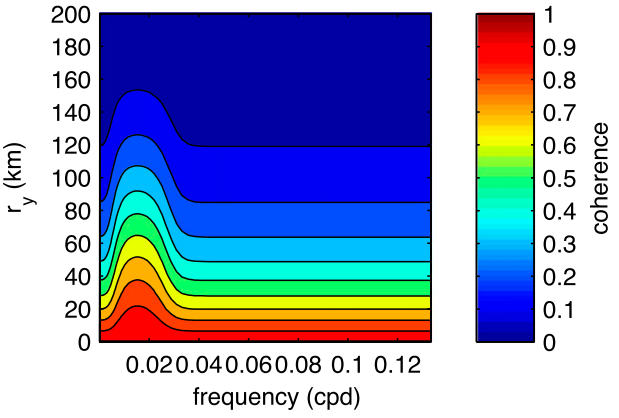

FIG. 16. Meridional velocity coherence as a function of meridional separation at 30°N, 190°E.

degree on the basis of known theories. Müller and Frankignoul (1981) present a detailed analysis of the frequency spectrum of the quasigeostrophic oceanic response to atmospheric forcing. The resulting spectrum is the integral response of the ocean to continuous random forcing by the atmosphere. Their predicted spectrum is white at low frequencies, changing smoothly to an ω^{-2} power law at $\omega \sim \omega_n^{\max}$ (their Fig. 7). The maximum frequency for the first baroclinic mode, $\omega_1^{\max} = \beta L_d/2$, depends on latitude primarily through the deformation radius L_d. Thus, they predict that the break point between the white low-frequency spectrum and ω^{-2} power law will decrease with latitude as the deformation radius decreases. The general shape predicted by Müller and Frankignoul (1981) is similar to the model frequency spectrum presented here.

For the wavenumber spectrum of total energy in the nth mode, Müller and Frankignoul (1981) predict

$$E_{\text{tot}}^n \sim \frac{1}{k^3 + kL_d^{-2}}. \tag{43}$$

For the baroclinic modes, the spectrum transitions from a k^{-1} power law at low wavenumber to a steeper k^{-3} at high wavenumber with the break point near the deformation radius. For the barotropic mode, the predicted spectrum is a k^{-3} power law at high wavenumber. This is steeper than the k^{-2} in the spectrum model presented here.

The character of balanced variability can also be attributed to quasigeostrophic (QG) turbulence theory. QG turbulence theory predicts a forward enstrophy cascade for wavenumbers higher than the

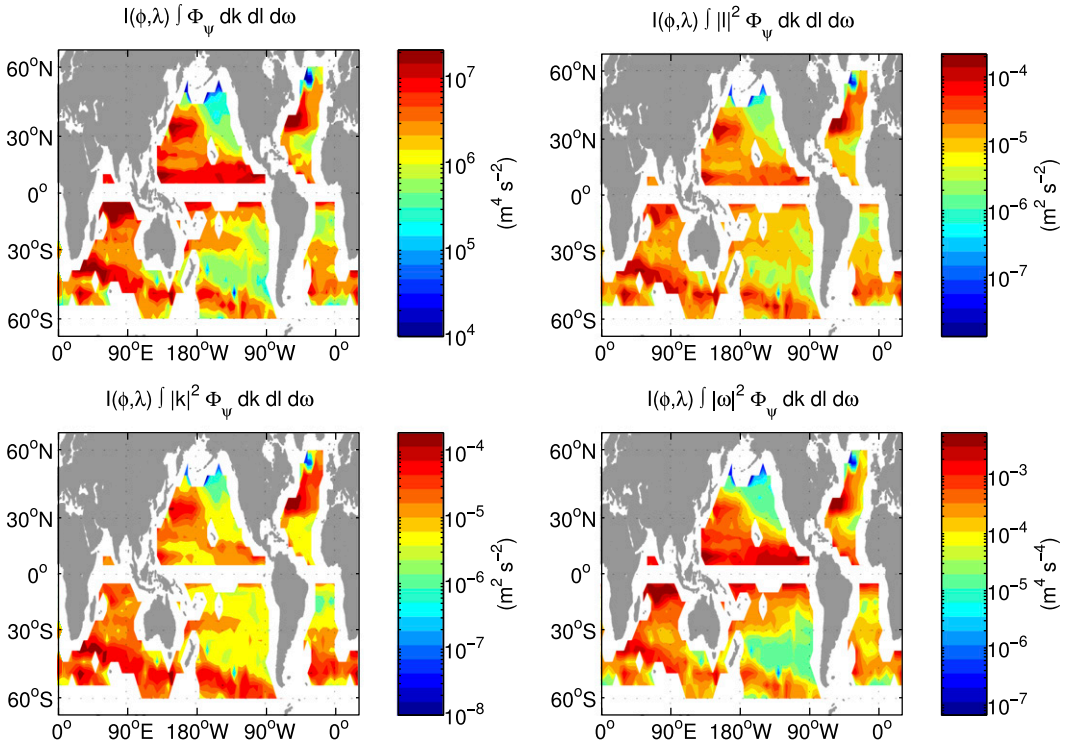

FIG. A1. Horizontally variable part of (A3) for (top left) $\tilde{p}$, $\tilde{\rho}$, $\tilde{\zeta}$, $\tilde{\theta}$, (top right) $\tilde{u}$, (bottom left) $\tilde{v}$, and (bottom right) $\tilde{w}$.

energy injection scale k_I (Charney 1971) and an inverse energy cascade for lower wavenumbers. The kinetic energy spectra in the forward and inverse ranges are

$$E(k) \sim k^{-3} \quad \text{for} \quad |k| > k_I \quad \text{and} \tag{44}$$

$$E(k) \sim k^{-5/3} \quad \text{for} \quad |k| < k_I. \tag{45}$$

For balanced motions, this requirement implies a k^{-5} power law for SSH for $|k| > k_I$ and $k^{-11/3}$ for $|k| < k_I$. The energy injection wavenumber appears to be close to the deformation scale (Scott and Wang 2005). A considerable literature compares observed wavenumber spectra with the predictions of turbulence theories (e.g., Stammer 1997; Le Traon et al. 2008; Lapeyre 2009; Wang et al. 2010; Xu and Fu 2012). Further, eddy generation through baroclinic instability has shown skill in predicting observed wavelengths of variability (Tulloch et al. 2011) and seasonal modulation of EKE (Qiu et al. 2008).

Some inconvenient evidence has been ignored here. Most important, the model assumes that variability is attributable to the superposition of a random wave field, excluding evidence for ''coherent motions'' (Chelton et al. 2011; Early et al. 2011). Structures such as isolated vortices, where present, would significantly increase the expected variance relative to a random wave field by phase-locking different horizontal wavelengths and frequencies. These effects could be addressed by estimating higher-order spectra, such as the bispectrum and trispectrum, which describe nonlinear interactions between spectral components.

Despite the shortcomings of the present model, it has reached a stage where it can be usefully applied in a variety of areas. Obvious applications include the estimation of uncertainties in observed trends, observing-system design, objective mapping of data, and evaluating the scales of variability produced in ocean GCMs.

Acknowledgments. We thank R. Ferrari, G. Flierl, and S. Jayne for helpful comments. Moored current-meter and temperature-sensor data were provided by R. Scott and D. Furnival through the Global Multi-Archive Current Meter Database. The altimeter products were produced by SSALTO/DUACS and distributed by AVISO, with support from CNES. This research was supported by NASA under Grants NNG06GC28G and NNX08AR33G.

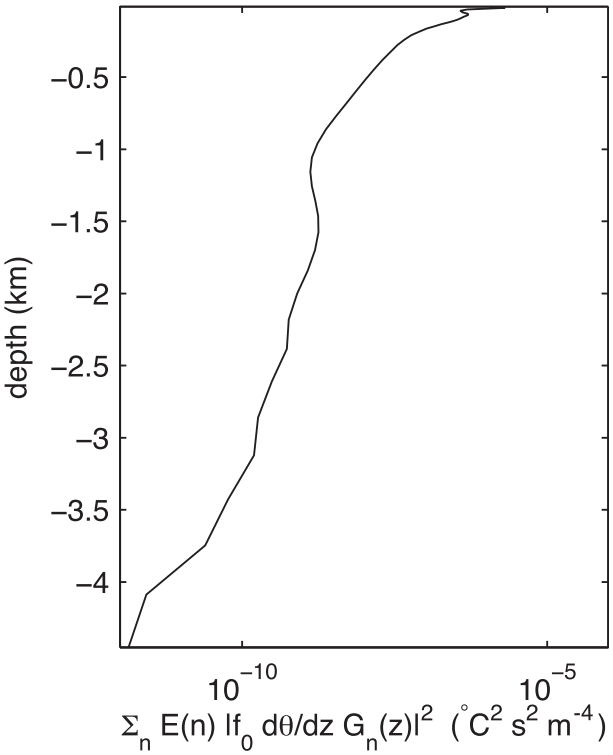

FIG. A2. Vertical structure part of (A3) for $\tilde{\theta}$ at 39°N, 230°E. Multiplying by the horizontally variable part shown in Fig. A1 gives the temperature variance.

APPENDIX

Working with the Spectrum Model

Although the shape of the spectrum model is easily computed from (30) integrated over frequency or wavenumber, calculating the absolute amplitude is more complicated. Here, we show by example how to use the spectrum model to predict quantitative values (e.g., variance) for different variables. The variance predicted by the spectrum model for a generic variable χ at depth z is

$$\sigma_\chi^2(z) = \int_0^\infty \int_{-\infty}^\infty \int_{-\infty}^\infty \Phi_\chi(k, l, \omega, z; \phi, \lambda)\, dk\, dl\, d\omega. \tag{A1}$$

By (17) and (20),

$$\sigma_\chi^2(z) = I(\phi, \lambda) \sum_n E(n) \int_0^\infty \int_{-\infty}^\infty \int_{-\infty}^\infty |\tilde{\chi}|^2 \Phi_\psi(k, l, \omega; \phi, \lambda)\, dk\, dl\, d\omega, \tag{A2}$$

where $\Phi_\psi(k, l, \omega; \phi, \lambda)$ is the three-dimensional spectrum model (30). The characteristic functions (8)–(14) are separable: $\tilde{\chi} = \hat{\chi}(k, l, \omega)\overline{\chi}(z)$, and we define $\hat{p} = \hat{\rho} = \hat{\zeta} = \hat{\theta} = 1$, $\hat{u} = l$, $\hat{v} = k$, and $\hat{w} = \omega$. All other factors are grouped with the vertical part $\overline{\chi}(z)$, for example, $\overline{\theta}(z) = i2\pi F_n(z)$. With this separation, the variance is

$$\sigma_\chi^2(z) = I(\phi,\lambda)\int_0^\infty\int_{-\infty}^{\infty}\int_{-\infty}^{\infty}|\hat{\chi}|^2\Phi_\psi(k,l,\omega;\phi,\lambda)\,dk\,dl\,d\omega \times \sum_n E(n)|\overline{\chi}|^2, \tag{A3}$$

where the first two factors are a horizontally varying intensity, and the last represents the vertical structure. (Horizontal variation in the vertical mode shape is implicit.)

Four possible maps of the horizontally varying part of (A3) exist, corresponding to the four functional forms of $\hat{\chi}$ (Fig. A1). These maps primarily reflect the variation in EKE through $I(\phi, \lambda)$ but also depend on the spatially variable shape of the spectrum through the parameters L_x, L_y, and T. The vertical structure part of (A3) depends on location and the specific variable.

As an example of the use of the spectrum model, maps in Fig. A1 can be combined with the appropriate vertical structure to estimate variability at a given depth. The vertical structure for temperature, $\sum_n E(n)|f_0 G_n(z)\,\partial\theta_0/\partial z|^2$, is shown in Fig. A2 near 39°N, 230°E. At this location and 500-m depth, $I\iiint\Phi_\psi\,dk\,dl\,d\omega = 1.4\times 10^6\,\mathrm{m^4\,s^{-2}}$ and $\sum E(n)|\overline{\theta}|^2 = 1\times 10^{-8}\,\mathrm{°C^2\,s^2\,m^{-4}}$ so that $\sigma_\theta(500\,\mathrm{m}) = 0.12$°C as in Fig. 11.

Coherence from the spectrum model is given by (26) and depends on $F_n(z)$ through the characteristic function and $I(\phi, \lambda)$ through (20), quantities that are difficult to compute in general. Using the separation $\tilde{\chi} = \hat{\chi}(k, l, \omega)\ \overline{\chi}(z, n)$ introduced above with (17) and (20), (26) is

$$\mathrm{Coh}(\omega; r_x, r_y, z, z') = C(z)\frac{\displaystyle\int_{-\infty}^{\infty}\int_{-\infty}^{\infty}\hat{\chi}\hat{\Upsilon}^*\Phi_\psi(k,l,\omega;\phi,\lambda)e^{i2\pi(kr_x+lr_y)}\,dk\,dl}{\sqrt{\left[\displaystyle\int_{-\infty}^{\infty}\int_{-\infty}^{\infty}|\hat{\chi}|^2\Phi_\psi(k,l,\omega;\phi,\lambda)\,dk\,dl\right]\left[\displaystyle\int_{-\infty}^{\infty}\int_{-\infty}^{\infty}|\hat{\Upsilon}|^2\Phi_\psi(k,l,\omega;\phi,\lambda)\,dk\,dl\right]}}, \tag{A4}$$

where

$$C(z) = \frac{\displaystyle\sum_{n=0}^{\infty}\overline{\chi}\overline{\Upsilon}^*E(n)}{\sqrt{\left[\displaystyle\sum_{n=0}^{\infty}|\overline{\chi}|^2E(n)\right]\left[\displaystyle\sum_{n=0}^{\infty}|\overline{\Upsilon}|^2E(n)\right]}} \tag{A5}$$

contains the depth dependence. In general, $C(z)$ depends on the vertical structure functions $F_n(z)$ and $G_n(z)$ and is difficult to compute. However, in the common case of autocoherence, $\chi = \Upsilon$ and $C(z) = 1$. In this case, the coherence can be computed from the spectrum model (30) and the $\hat{\chi}$ part of the characteristic function, integrated over all wavenumbers.

REFERENCES

Aoki, K., A. Kubokawa, H. Sasaki, and Y. Sasai, 2009: Midlatitude baroclinic Rossby waves in a high-resolution OGCM simulation. *J. Phys. Oceanogr.,* **39,** 2264–2279.

Arbic, B. K., R. B. Scott, G. R. Flierl, A. J. Morten, J. G. Richman, and J. F. Shriver, 2012: Nonlinear cascades of surface oceanic geostrophic kinetic energy in the frequency domain. *J. Phys. Oceanogr.,* **42,** 1577–1600.

Bobrovich, A. V., and G. M. Reznik, 1999: Planetary waves in a stratified ocean of variable depth. Part 2. Continuously stratified ocean. *J. Fluid Mech.,* **388,** 147–169.

Bretherton, F., R. Davis, and C. Fandry, 1976: A technique for objective analysis and design of oceanographic experiments applied to MODE-73. *Deep-Sea Res. Oceanogr. Abstr.,* **23,** 559–582, doi:10.1016/0011-7471(76)90001-2.

Charney, J. G., 1971: Geostrophic turbulence. *J. Atmos. Sci.,* **28,** 1087–1097.

Chelton, D. B., and M. G. Schlax, 1996: Global observations of oceanic Rossby waves. *Science,* **272,** 234–238.

——, R. A. de Szoeke, M. G. Schlax, K. El Naggar, and N. Siwertz, 1998: Geographical variability of the first baroclinic Rossby radius of deformation. *J. Phys. Oceanogr.,* **28,** 433–460.

——, M. G. Schlax, R. M. Samelson, and R. A. de Szoeke, 2007: Global observations of large oceanic eddies. *Geophys. Res. Lett.,* **34,** L15606, doi:10.1029/2007GL030812.

——, ——, and ——, 2011: Global observations of nonlinear mesoscale eddies. *Prog. Oceanogr.,* **91,** 167–216, doi:10.1016/j.pocean.2011.01.002.

Chiswell, S. M., and G. J. Rickard, 2008: Eulerian and Lagrangian statistics in the Bluelink numerical model and AVISO altimetry: Validation of model eddy kinetics. *J. Geophys. Res.,* **113,** C10024, doi:10.1029/2007JC004673.

Davis, R. E., 1982: On relating Eulerian and Lagrangian velocity statistics: Single particles in homogeneous flows. *J. Fluid Mech.,* **114,** 1–26, doi:10.1017/S0022112082000019.

de Szoeke, R. A., and D. B. Chelton, 1999: The modification of long planetary waves by homogeneous potential vorticity layers. *J. Phys. Oceanogr.,* **29,** 500–511.

Dewar, W. K., 1998: On ''too fast'' baroclinic planetary waves in the general circulation. *J. Phys. Oceanogr.,* **28,** 1739–1758.

Ducet, N., P.-Y. Le Traon, and G. Reverdin, 2000: Global high-resolution mapping of ocean circulation from TOPEX/POSEIDON and *ERS-1* and *-2*. *J. Geophys. Res.,* **105** (C8), 19 477–19 498.

Early, J. J., R. M. Samelson, and D. B. Chelton, 2011: The evolution and propagation of quasigeostrophic ocean eddies. *J. Phys. Oceanogr.,* **41,** 1535–1555.

Ferrari, R., and C. Wunsch, 2010: The distribution of eddy kinetic and potential energies in the global ocean. *Tellus,* **62,** 92–108.

Forget, G., 2010: Mapping ocean observations in a dynamical framework: A 2004–06 ocean atlas. *J. Phys. Oceanogr.,* **40,** 1201–1221.

Frankignoul, C., and P. Müller, 1979a: On the generation of geostrophic eddies by surface buoyancy flux anomalies. *J. Phys. Oceanogr.,* **9,** 1207–1213.

——, and ——, 1979b: Quasi-geostrophic response of an infinite β-plane ocean to stochastic forcing by the atmosphere. *J. Phys. Oceanogr.,* **9,** 104–127.

Ganachaud, A., 2003: Large-scale mass transports, water mass formation, and diffusivities estimated from World Ocean Circulation Experiment (WOCE) hydrographic data. *J. Geophys. Res.,* **108,** 3213, doi:10.1029/2002JC001565.

Garrett, C., and W. Munk, 1972: Space-time scales of internal waves. *Geophys. Fluid Dyn.,* **2,** 225–264.

——, and ——, 1975: Space-time scales of internal waves: A progress report. *J. Geophys. Res.,* **80** (3), 291–297.

Gill, A. E., 1982: *Atmosphere–Ocean Dynamics.* International Geophysics Series, Vol. 30, Academic Press, 662 pp.

Hughes, C. W., and S. D. P. Williams, 2010: The color of sea level: Importance of spatial variations in spectral shape for assessing the significance of trends. *J. Geophys. Res.,* **115,** C10048, doi:10.1029/2010JC006102.

Jacobs, G. A., C. N. Barron, and R. C. Rhodes, 2001: Mesoscale characteristics. *J. Geophys. Res.,* **106** (C9), 19 581–19 595.

Keller, J. B., and G. Veronis, 1969: Rossby waves in the presence of random currents. *J. Geophys. Res.,* **74** (8), 1941–1951.

Killworth, P. D., and J. R. Blundell, 1999: The effect of bottom topography on the speed of long extratropical planetary waves. *J. Phys. Oceanogr.,* **29,** 2689–2710.

——, and ——, 2004: The dispersion relation for planetary waves in the presence of mean flow and topography. Part I: Analytical theory and one-dimensional examples. *J. Phys. Oceanogr.,* **34,** 2692–2711.

——, and ——, 2005: The dispersion relation for planetary waves in the presence of mean flow and topography. Part II: Two-dimensional examples and global results. *J. Phys. Oceanogr.,* **35,** 2110–2133.

——, and ——, 2007: Planetary wave response to surface forcing and instability in the presence of mean flow and topography. *J. Phys. Oceanogr.,* **37,** 1297–1320.

——, D. B. Chelton, and R. A. de Szoeke, 1997: The speed of observed and theoretical long extratropical planetary waves. *J. Phys. Oceanogr.,* **27,** 1946–1966.

LaCasce, J. H., 2012: Surface quasigeostrophic solutions and baroclinic modes with exponential stratification. *J. Phys. Oceanogr.,* **42,** 569–580.

Lapeyre, G., 2009: What vertical mode does the altimeter reflect? On the decomposition in baroclinic modes and on a surface-trapped mode. *J. Phys. Oceanogr.,* **39,** 2857–2874.

——, and P. Klein, 2006: Dynamics of the upper oceanic layers in terms of surface quasigeostrophy theory. *J. Phys. Oceanogr.,* **36,** 165–176.

Le Traon, P.-Y., 1990: Time scales of mesoscale variability and their relationship with space scales in the North Atlantic. *J. Mar. Res.,* **49,** 467–492, doi:10.1357/002224091784995828.

——, P. Klein, B. L. Hua, and G. Dibarboure, 2008: Do altimeter wavenumber spectra agree with the interior or surface quasi-geostrophic theory? *J. Phys. Oceanogr.,* **38,** 1137–1142.

Lin, X., J. Yang, D. Wu, and P. Zhai, 2008: Explaining the global distribution of peak-spectrum variability of sea surface height. *Geophys. Res. Lett.,* **35,** L14602, doi:10.1029/2008GL034312.

McWilliams, J. C., and G. R. Flierl, 1979: On the evolution of isolated, nonlinear vortices. *J. Phys. Oceanogr.,* **9,** 1155–1182.

Menemenlis, D., J.-M. Campin, P. Heimbach, C. Hill, T. Lee, A. Nguyen, M. Schodlok, and H. Zhang, 2008: ECCO2: High resolution global ocean and sea ice data synthesis. *Mercator Ocean Quarterly Newsletter,* No. 31, Mercator Ocean, Ramonville Saint-Agne, France, 13–21.

MODE Group, 1978: The Mid-Ocean Dynamics Experiment. *Deep-Sea Res.,* **25,** 859–910, doi:10.1016/0146-6291(78)90632-X.

Müller, P., and C. Frankignoul, 1981: Direct atmospheric forcing of geostrophic eddies. *J. Phys. Oceanogr.,* **11,** 287–308.

Müller, T. J., and G. Siedler, 1992: Multi-year current time series in the eastern North Atlantic Ocean. *J. Mar. Res.,* **50,** 63–98.

Philander, S. G. H., 1978: Forced oceanic waves. *Rev. Geophys.,* **16,** 15–46.

Qiu, B., R. B. Scott, and S. Chen, 2008: Length scales of eddy generation and nonlinear evolution of the seasonally modulated South Pacific subtropical countercurrent. *J. Phys. Oceanogr.,* **38,** 1515–1528.

Rhines, P. B., and F. P. Bretherton, 1973: Topographic Rossby waves in a rough-bottomed ocean. *J. Fluid Mech.,* **61,** 583–607.

Roden, G., 2005: Shipboard acoustic Doppler current profiling during cruise TT9306 (SAC ID 00016). Pangaea online dataset, doi:10.1594/PANGAEA.319488.

Samelson, R. M., 1992: Surface-intensified Rossby waves over rough topography. *J. Mar. Res.,* **50,** 367–384.

Scharffenberg, M., and D. Stammer, 2010: Seasonal variations of the large-scale geostrophic flow field and eddy kinetic energy inferred from the TOPEX/Poseidon and *Jason-1* tandem mission data. *J. Geophys. Res.,* **115,** C02008, doi:10.1029/2008JC005242.

Scott, R. B., and F. Wang, 2005: Direct evidence of an oceanic inverse kinetic energy cascade from satellite altimetry. *J. Phys. Oceanogr.,* **35,** 1650–1666.

——, B. K. Arbic, E. P. Chassignet, A. C. Coward, M. Maltrud, A. Srivivasan, and A. Varghese, 2010: Total kinetic energy in three global eddying ocean circulation models and over 5000 current meter records. *Ocean Modell.,* **32** (3–4), 157–169.

Stammer, D., 1997: Global characteristics of ocean variability estimated from regional TOPEX/POSEIDON altimeter measurements. *J. Phys. Oceanogr.,* **27,** 1743–1769.

Tailleux, R., and J. C. McWilliams, 2001: The effect of bottom pressure decoupling on the speed of extratropical, baroclinic Rossby waves. *J. Phys. Oceanogr.,* **31,** 1461–1476.

Taylor, G. I., 1921: Diffusion by continuous movements. *Proc. London Math. Soc.,* **20,** 196–211.

Tulloch, R., J. Marshall, C. Hill, and K. S. Smith, 2011: Scales, growth rates and spectral fluxes of baroclinic instability in the ocean. *J. Phys. Oceanogr.,* **41,** 1057–1076.

Vanmarcke, E., 2010: *Random Fields: Analysis and Synthesis.* World Scientific, 364 pp.

Vanneste, J., 2003: Nonlinear dynamics over rough topography: Homogeneous and stratified quasi-geostrophic theory. *J. Fluid Mech.,* **474,** 299–318.

Wang, D.-P., C. N. Flagg, K. Donohue, and H. T. Rossby, 2010: Wavenumber spectrum in the Gulf Stream from shipboard

ADCP observations and comparison with altimetry measurements. *J. Phys. Oceanogr.,* **40,** 840–844, doi:10.1175/2009JPO4330.1.

Wortham, C., 2013: A multi-dimensional spectral description of ocean variability with applications. Ph.D. thesis, MIT/WHOI Joint Program, 184 pp.

Wunsch, C., 1997: The vertical partition of oceanic horizontal kinetic energy. *J. Phys. Oceanogr.,* **27,** 1770–1794.

——, 1999: A summary of North Atlantic baroclinic variability. *J. Phys. Oceanogr.,* **29,** 3161–3166.

——, 2006*: Discrete Inverse and State Estimation Problems with Geophysical Fluid Applications.* Cambridge University Press, 384 pp.

——, 2008: Mass and volume transport variability in an eddy-filled ocean. *Nat. Geosci.,* **1,** 165–168.

——, 2009: The oceanic variability spectrum and transport trends. *Atmos.–Ocean,* **47** (4), 281–291.

——, 2010: Toward a mid-latitude ocean frequency-wavenumber spectral density and trend determination. *J. Phys. Oceanogr.,* **40,** 2264–2281.

——, and D. Stammer, 1995: The global frequency-wavenumber spectrum of oceanic variability estimated from TOPEX/POSEIDON altimetric measurements. *J. Geophys. Res.,* **100** (C12), 24 895–24 910.

Xu, Y., and L.-L. Fu, 2012: The effects of altimeter instrument noise on the estimation of the wavenumber spectrum of sea surface height. *J. Phys. Oceanogr.,* **42,** 2229–2233.

Zang, X., 2000: Spectral description of low frequency oceanic variability. Ph.D. thesis, MIT/WHOI Joint Program, 187 pp.

——, and C. Wunsch, 2001: Spectral description of low-frequency oceanic variability. *J. Phys. Oceanogr.,* **31,** 3073–3095.

Zhai, X., H. L. Johnson, and D. P. Marshall, 2011: A model of Atlantic heat content and sea level change in response to thermohaline forcing. *J. Climate,* **24,** 5619–5632.